INL/RPT-22-67887

Development of a Subchannel Capability for Liquid-Metal Fast Reactors in Pronghorn

June 2022

Nuclear Energy Advanced Modeling and Simulation M2 Milestone

Mauricio Tano[1], Sebastian Schunert[1], Vasileios Kyriakopoulos[2], Aydin Karahan[3], and April Novak[3]

[1]*Idaho National Laboratory*
[2]*Department of Nuclear Engineering, Texas A&M University*
[3]*Argonne National Laboratory*

Idaho National Laboratory

INL is a U.S. Department of Energy National Laboratory operated by Battelle Energy Alliance, LLC

INL/RPT-22-67887

Development of a Subchannel Capability for Liquid-Metal Fast Reactors in Pronghorn

Nuclear Energy Advanced Modeling and Simulation M2 Milestone

Mauricio Tano[1], Sebastian Schunert[1], Vasileios Kyriakopoulos[2], Aydin Karahan[3], and April Novak[3]

[1]**Idaho National Laboratory**
[2]**Department of Nuclear Engineering, Texas A&M University**
[3]**Argonne National Laboratory**

June 2022

Idaho National Laboratory
Idaho Falls, Idaho 83415

http://www.inl.gov

Prepared for the
U.S. Department of Energy
Office of _____
Under DOE Idaho Operations Office
Contract DE-AC07-05ID14517

Page intentionally left blank

ABSTRACT

This report details the development and demonstration of an entirely new capability in Pronghorn, namely the ability to model liquid-metal fast reactor (LMFR) flow conditions on the engineering scale. We developed two modeling approaches for LMFR that can be used separately or be combined into a hybrid simulation:

- a modern subchannel capability called Pronghorn-Subchannel for square and hexagonal lattices
- a porous flow capability for LMFR geometries.

The report emphasises the novel aspects of the developed subchannel capability and the interoperability of the subchannel capability, porous flow capability, and multiphysics tools within the multiphysics object oriented simulation environment (MOOSE). Here we demonstrate the ability to:

- Accurately model subchannel flow in hexagonal lattices
- Couple the subchannel flow model to multidimensional finite-element method (FEM) or finite-volume method (FVM) heat conduction models
- Model LMFRs using Pronghorn's porous media FVM approach
- Couple porous flow FVM and subchannel models in a single simulation
- Explicitly model inter-wrapper flows along with conjugate heat transfer from the intra-element flow
- Demonstrate the numerical robustness of the subchannel algorithm by simulating intra-element flow recirculation in a high-buoyancy, low-flow fuel element.

Page intentionally left blank

CONTENTS

FIGURES

TABLES

ACRONYMS

ABTR	Advanced Burner Test Reactor
CFD	Computational Fluid Dynamics
DoF	degrees of freedom
FEM	finite-element
FFM	fuel failure mockup
FVM	finite volume method
JFNKM	Jacobian-free Newton-Krylov method
LMFR	liquid-metal fast reactor
MOOSE	Multiphysics Object-Oriented Simulation Environment
ORNL	Oak Ridge National Laboratory
PDE	partial differential equation
PETSc	Portable, Extensible Toolkit for Scientific Computation
PrSub	Pronghorn-Subchannel
SFR	sodium fast reactor
V&V	verification and validation
VBV	verification, numerical benchmarking, validation

Page intentionally left blank

1. Introduction

This report details the development and demonstration of an entirely new capability in Pronghorn, namely the ability to model liquid-metal fast reactor (LMFR) flow conditions on the engineering scale. We developed two modeling approaches for LMFRs that can be used separately or be combined into a hybrid simulation:

- a modern subchannel capability called Pronghorn-Subchannel (PrSub) for square and hexagonal lattices
- a porous flow capability for LMFR geometries.

The report emphasises the novel aspects of the developed subchannel capability and the interoperability of the subchannel capability, porous flow capability, and multiphysics tools within the Multiphysics Object-Oriented Simulation Environment (MOOSE) framework.

PrSub allows for the efficient simulation of steady-state and transient LMFR flow conditions during normal and off-normal conditions (a test case with 217 pins and an overall 300,000 degrees of freedom (DoF) completes a time step in about 90 seconds on a single CPU on a laptop). Several features of the developed subchannel code surpass the capabilities available in legacy codes, such as:

- The ability to couple to general geometry heat structures
- A flexible and robust solution algorithms based on Portable, Extensible Toolkit for Scientific Computation (PETSc) that allows solving problems that are challenging to traditional subchannel solvers.

Examples for challenging flow conditions in LMFRs are (1) recirculation in fuel elements caused by strong buoyancy forces (demonstrated in this work) and (2) partial or full flow blockage (demonstrated as proof of principle and under development in PrSub, respectively).

In addition to PrSub, we developed a porous flow capability for LMFRs to allow the coarse-mesh modeling of large portions of LMFR reactor cores and coupling them to neutronics and deformation calculations.

PrSub leverages the infrastructure available in the MOOSE framework to allow for seamless embedding of subchannel models in the wider context of MOOSE multiphysics models. This capability is exercised in this report to model the flow conditions in the inter-wrapper space using Pronghorn's finite volume method (FVM) models, while solving intra-wrapper flow using a subchannel model. Explicitly modeling inter-wrapper flows is intended to improve on the equivalent thermal conductivity approach widely used throughout the LMFR community.

In summary, the following capabilities were developed for completion of this milestone and are demonstrated in this report:

- Implement, verify, and validate closure relations for hexagonal lattices
- Couple the subchannel flow model to multidimensional finite-element (FEM) or FVM heat conduction models and iterating to consistency via fixed point iterations.
- Develop closure relationships for modeling LMFRs using Pronghorn's porous media FVM approach
- Model LMFRs using a mixed FVM porous flow and subchannel approach
- Explicitly model inter-wrapper flows along with conjugate heat transfer from the intra-element flow to and from the duct to the inter-wrapper flow using Pronghorn's FVM capabilities
- Propose a simple approach to model special assemblies, such as double-ducted control assemblies, using Pronghorn's FVM porous flow model
- Scale up to about 37 assemblies discretized with about $120,000$ elements in three-dimensional geometry using Pronghorn's FVM solver, and further increasing the problem size requires removing current inefficiencies in the FVM solution algorithm.

Additional effort is required to bring portions of the described capability to production level. The most pressing of these issues is to reduce both the execution time and memory consumption of Pronghorn's FVM solver. Currently, the porous flow equations are solved using Newton's method with a direct linear solver to solve the linear system at each Newton iteration. This method does not scale well beyond small problem sizes and poses significant issues even for moderately

sized problems in three spatial dimensions. MOOSE is currently being refactored to enable the implementation of efficient segregated solvers. Until these framework changes are complete, the achievable problem size for Pronghorn FVM remains limited.

Most capabilities reported in this work are demonstrated for conceptual test cases. Bringing the LMFR capability in Pronghorn to the production level requires demonstration and verification, numerical benchmarking, validation (VBV) for realistic test cases. The notable exception is the completion of Oak Ridge National Laboratory (ORNL)'s 19-pin and Toshiba's 37-pin subchannel benchmarks with the subchannel solver. The LMFR porous flow capability, the coupled subchannel-porous flow model, and the subchannel model of flow inversion require further assessment and verification and validation (V&V).

We organize this work as follows. Section 2 briefly describes the codes included in this report and introduces jargon used throughout this report. Then, Section 3 describes the subchannel governing equations, solution methodology, and closure models along with the porous media model for LMFRs and the closure correlations used in this porous approach. In Section 4 and 5, we describe the results of two V&V exercises, namely ORNL's 19-pin and Toshiba's 37-pin benchmarks. We then present results demonstrating the modeling capabilities for LMFRs in Sections 6 and 7. Section 6 introduces the results obtained for a porous flow core model with Pronghorn FVM, including results for a seven assembly and 37 assembly mini-core model, with control and fuel assemblies and characteristics similar to the Advanced Burner Test Reactor (ABTR). Then, the temperature fields obtained in the outside wall of the wrapper in the 37 assembly core model are applied as a boundary condition for a coupled, ABTR-inspired fuel assembly model that includes wrapper, subchannel, and fuel pins. The three analyses we performed include an estimated nominal mass flow rate and a low mass flow rate in steady-state conditions and a transient analysis involving a power burst in one of the fuel assemblies. Finally, an online coupling case between PrSub and Pronghorn FVM is presented for the seven assembly mini-core model.

2. Codes and Code Jargon

The focus of this work is the development of an LMFR fluid simulation capability within the Nuclear Energy Advanced Modeling and Simulation engineering-scale toolkit. The four codes we used are:

- The MOOSE framework [6] is an open-source framework for discretizing partial differential equations (PDEs) using the FEM and FVM methods. MOOSE provides a plug-in infrastructure for various FEM and FVM simulation components, such as kernels (PDEterms), boundary conditions (PDEterms on boundaries), timestepping algorithms, general purpose objects (*UserObjects*) that the user can customize to do any desired task, etc. MOOSE is extensible by the community, encouraging contributions to the code base but allowing developers to build their own applications without contributing the code back to MOOSE; in fact, the MOOSE design allows researchers to harness all the objects in the framework in derived or MOOSE-based applications, which are commonly named after animals. In addition, MOOSE defines a custom syntax that allows a composition of complex multiphysics problems within the input file. MOOSE supports hybrid parallelism (*mpi* and threading) and scales well into the range of thousands of processors without exposing the complexity of the parallel communication to the average code contributor.

- Pronghorn [7] is a MOOSE-based, coarse-mesh thermal-hydraulics code that solves porous-medium fluid mechanics, heat transfer, and heat conduction equations for problems where the complicated geometry and interaction between fluid and solid is treated in an average sense via appropriate correlations. Pronghorn is capable of modeling steady-state and transient conditions in gas and salt-cooled pebble-bed reactors and molten-salt reactors. This work extends Pronghorn capabilities to LMFRs.

- PrSub [3] is a Pronghorn module that solves subchannel equations in square and hexagonal lattices for single-phase fluids and is discussed in detail in this work.

- Bison [8] is a 3D FEM-based nuclear fuel performance code applicable to a variety of fuel forms, including light-water reactor fuel rods, tristructural isotropic particle fuel,

and metallic rod and plate fuel. It is a multiphysics fuel analysis tool that solves fully coupled thermomechanical problems. Bison is also based on the MOOSE framework [9] and implicitly solves coupled thermomechanical equations over the domain of a single fuel rod using the Jacobian-free Newton-Krylov method (JFNKM)[10]. The coupling of PrSub and Bison, and potentially a neutronics code, will provide a multiphysics framework for a full reactor core analysis. The Bison governing equations consist of fully coupled partial differential equations for energy, species, and momentum conservation. The energy balance is given in terms of heat conduction, see Equation (1).

$$\rho c_p \frac{\partial T}{\partial t} + \vec{\nabla} \cdot \vec{q} - E_f \dot{F} = 0, \tag{1}$$

where T, ρ, and c_p are the temperature, density, and specific heat capacity, respectively, E_f is the energy released in a single fission event, and $\dot{F}$ is the volumetric fission rate. The product gives the volumetric heat source. The heat flux is given in Equation 2.

$$\vec{q} = -k\vec{\nabla}T, \tag{2}$$

where k denotes the thermal conductivity of the material. $\dot{F}$ can be an input from a separate neutronics calculation (such as Griffin [11]) or computed based on rod average power and axial profile data.

In addition, the following jargon is used throughout the report:

- Nonlinear variable: a variable that MOOSE solves for via the standard PETSc interface provided in MOOSE. Nonlinear variables reside in the nonlinear system and are only set by MOOSE's internal solution machinery. They can be of different types, including linear continuous (*linear Lagrange*) and constant discontinuous variables (*constant monomial*).
- Auxiliary variable: all variables that are not nonlinear variables. They offer great flexibility and can be set by auxiliary kernels, transfers, or initial conditions.
- Multi-app: a system [12] that allows a MOOSE app (the *primary app*) to create additional independent MOOSE apps (the *secondary apps*) executed at user-defined points during the

primary app's execution. Multi-apps can be used to create loose or Picard-type coupled equation systems. Multi-apps are flexible in the sense that a secondary app can have its own "tertiary" apps. In this way, researchers can create arbitrary trees of MOOSE apps.

- Multi-app transfer: objects that transfer information between different apps in the multi-app tree.

- Fully coupled: all variables are solved in a single system of nonlinear equations using either Newton's or a quasi-Newton method.

- Strongly coupled: equations are split into at least two groups and solved sequentially while passing information between each other after each solution step. The term strongly coupled is usually used interchangeably with Picard iterations. However, the implication of strongly coupled equations in MOOSE jargon is that the multi-app system is used for setting up the system of equations. It is possible to use quasi-Newton methods in strongly coupled problems, and therefore, it is not strictly identical to Picard-type coupling.

- Verification: confirming that the code correctly solves equations; verification includes comparison to analytical results or the method of manufactured solutions.

- Numerical benchmarking: essentially a code-to-code comparison of results for well defined numerical benchmarks that can be performed between codes of identical fidelity levels (subchannel compared with other subchannel codes) or between different fidelity levels (subchannel compared to direct numerical simulation results).

- Validation: confirming that the code correctly solves the problem, which requires a comparison to experimental data to ensure the set of equations, assumptions, and correlations describe the physical problem of interest well. The validation for multiphysics problems related to LMFRs is hindered by the lack of validation data. Therefore, verification and numerical benchmarking are often the only avenues for code developers to build confidence in their codes.

3. Theory

The section is divided into two parts. First, we detail the theoretical aspects of the formulation, solution, and closure correlations for the subchannel problem and then present the porous media formulation with adapted closure correlations for LMFRs.

3.1 The Subchannel Method

In this section, we describe the approach for solving the subchannel equations that we adopted in this work. The description includes the governing equations, the closure models used for the friction and heat exchange factors, and the algorithm used to solve the subchannel equations.

3.1.1 Subchannel Governing Equations

The subchannel thermal-hydraulic analysis is based on the conservation equations of mass, linear momentum, and energy on control volumes located between the rods of the reactor assembly as shown in Figure 1 [1, 2]. For simplicity, a square control volume is presented on this figure, but an equivalent control volume can be defined between the rods of triangular or hexagonal assemblies used in LMFRs.

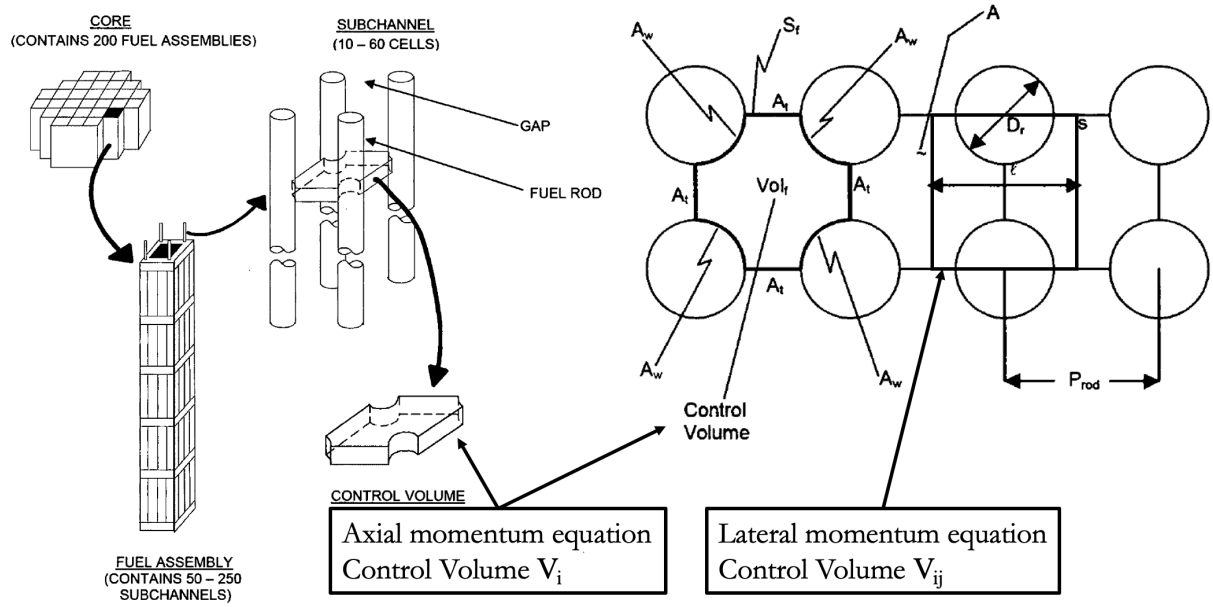

Figure 1: Square lattice subchannel control volumes [1, 2].

Control volumes communicate with neighboring control volumes in both axial and lateral directions, capturing the three-dimensional flow field in a nuclear reactor. Starting from the continuum formulation for the conservation of mass, momentum, and energy equations [13], we integrate over a control volume V_i to obtain the subchannel equations for the conservation of mass, energy, and linear momentum in the axial direction and over a transversal volume V_{ij} to obtain the conservation equation for linear momentum in the lateral direction.

All results presented in this work are obtained using PrSub's *collocated formulation* (velocities and pressures reside in the same cell centers). In addition to the collocated formulation, PrSub supports a *staggered formulation* of mass and momentum in the axial direction in which the linear momentum equation is integrated over a volume $\tilde{V}_i$, which is axially shifted with respect to V_i by half a control volume height. We have observed little difference in performance and accuracy between the collocated and staggered grid algorithms on the test cases presented in this work. Hence, all cases use the collocated mass-momentum formulation. The reader is referred to Reference [1] for further details about the collocated grid formulation.

The subchannel equations solved by PrSub are:

- **Conservation of mass**:

$$\frac{\partial \rho_i}{\partial t} V_i + \Delta \dot{m}_i + \sum_j w_{ij} = 0, \tag{3}$$

  where i is the subchannel index, j is the index of the neighbor subchannel, Δ refers to the difference between the inlet and outlet of the control volume in the axial direction, $\dot{m}_i[kg/sec]$ is the mass flow rate of subchannel i in the axial direction, ρ_i is the density, and $w_{ij}[kg/sec]$ is the diversion cross flow in the lateral direction from subchannel i to neighboring subchannel j, resulting from local pressure differences between the two subchannels.

- **Conservation of linear momentum in the axial direction**:

$$\frac{\partial \dot{m}_i}{\partial t} \Delta Z + \Delta \left(\frac{{\dot{m}_i}^2}{S_i^z \rho_i} \right) + \sum_j w_{ij} U^\star = -S_i \Delta P_i + Friction_i + Drag_{ij} - g \rho_i S_i \Delta Z. \tag{4}$$

  On the left-hand side, we collect the change of momentum in the axial direction $\Delta(\frac{{\dot{m}_i}^2}{S_i^z \rho_i})$ and the momentum transfer between subchannels due to diversion cross flow $\sum_j w_{ij} U^\star$. U^* is

the axial velocity of the donor cell, which is interpolated to the center of the control volume V_i, and $-g\rho_i S_i \Delta Z$ is the force exerted by gravity, where g is the gravitational acceleration, S_i is the flow area, and ΔZ the axial length of the control volume V_i. We have assumed that gravity is the only significant body force in the momentum equation but other forces can be easily integrated into our subchannel formulation. The donor cell is the cell the cross flow flows out; it is determined by the sign of w_{ij}. If it is positive, the donor cell is i, and if it is negative, the donor cell is j. Henceforward, donor cell quantities will be denoted with the star (*) symbol. $Friction_i$ represents irreversible pressure drops caused by the interaction between the fluid and the solid structures, including the possible local form loss coefficient due to spacers and mixing vanes. $Friction_i$ is computed from correlations adapted to the particular assembly geometry. $Drag_{ij}$ is caused by viscous stresses within the fluid at the interface between subchannels and is also computed from closure correlations. Finally, ΔP_i is the axial pressure drop at volume V_i.

- **Conservation of linear momentum in the lateral direction**:

$$\frac{\partial w_{ij}}{\partial t} L_{ij} + \frac{L_{ij}}{\Delta Z} \Delta (w_{ij} \bar{U}_{ij}) = \; - S_{ij} \Delta P_{ij} + Friction_{ij}. \tag{5}$$

Here, $S_{ij} = g_{ij} \Delta z$ is the lateral flow surface area between the subchannels i,j, g_{ij} is the gap between subchannels, $(\Delta P_{ij} / L_{ij})$ is the lateral pressure gradient across the subchannels, L_{ij} is the distance between the centers of subchannels i,j, and $\bar{U}_{ij}$ is the interpolated average axial velocity at the center of the two subchannels. The overall friction loss term $Friction_{ij}$ absorbs all the viscous effects and form losses associated with momentum exchange between the fluid and the wall due to the fluid motion through the gap or mixing grids and requires closure correlations.

- **Conservation of enthalpy:**

$$\frac{\partial \langle \rho h \rangle_i}{\partial t} V_i + \Delta (\dot{m}_i h_i) + \sum_j w_{ij} h^\star + h'_{ij} = q'_i \Delta Z - \sum_j Y_{ij} \frac{S_{ij} \eta_{ij}}{L_{ij}} (T_i - T_j) + \frac{1}{\Delta Z} \Delta (Y_i S_i T_i). \tag{6}$$

Here, we have defined h'_{ij} as the turbulent enthalpy transfer between subchannels i and j, q'_i as the average linear power $[\frac{W}{m}]$ going into the control volume of subchannel i from the fuel rods, T_i as the temperature of subchannel element i, $Y[\frac{W}{m.K}]$ as the thermal conductivity of the coolant and its index that indicate the position in which it should be computed, and η_{ij} as the radial conduction factor yielding the effective conduction length between channels i and j. The second-to-last term in the right-hand side captures heat conduction in the radial direction while the last one captures heat conduction in the axial direction. For a single-phase liquid, we can neglect dissipation due to viscous stresses and set the total derivative of pressure (work of pressure) to zero. We can also neglect the volumetric heat source due to moderation, since heat is mainly transferred to the fluid through the rod surfaces.

3.1.2 Interpolation Schemes

As seen in the previous section, some of the variables must be interpolated to the center of the subchannel cells in the axial direction. When using fine meshes, the interpolation scheme has little impact on the results. However, when using coarse meshes in the axial direction for a fast-running subchannel solver, the interpolation scheme has a larger impact. The standard interpolation scheme for a dummy variable ϕ in the axial direction reads as follows:

$$\phi_{i+1/2} = \alpha_i \phi_i + (1 - \alpha_i)\phi_{i+1} \tag{7}$$

where $i + 1/2$ is the position at the center of the cell, i is the one at its bottom face, $i + 1$ is the one at the top, and α_i is the interpolation coefficient. For an ascending flow in LMFRs, one may upwind these quantities without finding artificial solutions or detriments in numerical performance. However, the situation is more complicated in monotonic flow configurations, such as the ones found in recirculating flows for low-flow assemblies. In this case, a standard upwind will lead to physically incorrect results. For this purpose, the subchannel supports five different interpolation schemes:

- Standard upwind:

$$\alpha_i = 1.0\,, \tag{8}$$

- Standard downwind:

$$\alpha_i = 0.0\,, \tag{9}$$

- Selective upwind:

$$\alpha_i = \begin{cases} 1.0 & \text{if } \phi_i \geq 0 \\ 0.0 & \text{if } \phi_i < 0 \end{cases}, \tag{10}$$

- Central difference:

$$\alpha_i = \frac{1}{2}\,, \tag{11}$$

- Exponential scheme:

$$\alpha_i = \frac{(Pe-1)e^{Pe}+1}{Pe(e^{Pe}-1)}\,, \tag{12}$$

where Pe is the Peclet number in the axial direction defined as $Pe = \frac{\Delta(\frac{\dot{m}_i^2}{S_i^2\rho_i})}{Friction_i}$. In practice, for flow configurations with a high influence of cross flows and with recirculation, the exponential scheme has proven to be the most robust numerically. However, due to the larger number of operations involved, it slightly deteriorates the performance of the code. For most cases, the numerical performance of central difference was reasonable and did not yield a large difference with respect to the exponential scheme. The selective upwind schemes were generally highly diffusive and their usage is not recommended for coarse meshes. For ascending (respectively descending) flow configurations, all schemes perform approximately equally, except for the downwind (upwind) one.

3.1.3 Geometric Parameters for Subchannel Grids

For square grids, which don't involve wire spacers, the definition of the subchannel geometry is straightforward. The reader is referred to [1] for details about this geometry. However, we implemented a special geometric treatment for triangular subchannel lattices. Geometric parameters, such as flow area, wetted perimeter, subchannel equivalent diameter, are defined for the bare and wire-wrapped fuel bundle conditions used in the equations below. Subindices 1, 2, and 3 correspond to inner, edge, and corner subchannel types, respectively. We first defined P as the pitch, W as the gap between fuel rods and duct, D as the fuel rod diameter, D_w as the

wire diameter, θ as the wire angle, H as the wire lead length, A is the flow area, P_w as the wetted perimeter, D_e is the equivalent diameter, and the prime superscript ($'$) is used for bare bundles throughout the section. Using this nomenclature, the geometric parameters for square grids are defined as follows:

- Bare rod flow area and wetted perimeter:

$$A_1' = \frac{\sqrt{3}}{4}P^2 - \frac{\pi D^2}{8}, \tag{13}$$

$$A_2' = P(W - \frac{D}{2}) - \frac{\pi D^2}{8}, \tag{14}$$

$$A_3' = \frac{(W - \frac{D}{2})^2}{\sqrt{3}} - \frac{\pi D^2}{24}, \tag{15}$$

$$P_{w1}' = \frac{\pi D}{2}, \tag{16}$$

$$P_{w2}' = P + \frac{\pi D}{2}, \tag{17}$$

$$P_{w3}' = \frac{\pi D}{6} + \frac{2(W - \frac{D}{2})}{\sqrt{3}}, \tag{18}$$

- Wire-wrapped flow area and wetter perimeter:

$$A_1 = A_1' - \frac{\pi D_w^2}{8\cos(\theta)}, \tag{19}$$

$$A_2 = A_2' - \frac{\pi D_w^2}{8\cos(\theta)}, \tag{20}$$

$$A_3 = A_3' - \frac{\pi D_w^2}{24\cos(\theta)}, \tag{21}$$

$$P_{w1} = P_{w1}' - \frac{\pi D_w}{2\cos(\theta)}, \tag{22}$$

$$P_{w2} = P_{w2}' - \frac{\pi D_w}{2\cos(\theta)}, \tag{23}$$

$$P_{w3} = P_{w3}' - \frac{\pi D_w}{6\cos(\theta)}, \tag{24}$$

$$\cos(\theta) = \frac{H}{\sqrt{H^2 + (\pi(D + D_w))^2}}, \tag{25}$$

- Wire projected Area:

$$A_{r1} = \pi(D + D_w)\frac{D_w}{6}, \tag{26}$$

$$A_{r2} = \pi(D + D_w)\frac{D_w}{4}, \tag{27}$$

$$A_{r3} = \pi(D + D_w)\frac{D_w}{6}, \tag{28}$$

- Bare rod flow hydraulic diameter:

$$D'_{ei} = \frac{4A'_i}{P'_{wi}}, \tag{29}$$

- Wire-wrapped flow hydraulic diameter:

$$D_{ei} = \frac{4A_i}{P'_{wi}}, \tag{30}$$

These geometric coefficients allow us to define adapted closure correlations for wire-wrapper triangular lattices in the next section.

3.1.4 Closure Models

Computational Fluid Dynamics (CFD) resolves the entire geometry, and hence, pressure drop and mixing arise naturally from the solution of the high-fidelity system of equations. However, the subchannel formulation considers only one control volume between rods, and hence, closure models are required for computing axial and lateral friction, form losses and turbulent mixing in the lateral direction, and the conduction factor. Moreover, when structures are included in the subchannel formulation (e.g., fuel pins or ducts in LMFRs), heat exchange coefficient correlations are required to compute the heat transfer between the fluid and the structures. The closure models currently included in our subchannel formulation are detailed below.

- Axial direction friction term:

$$Friction_i = -\frac{1}{2}\Xi_i \frac{\dot{m}_i|\dot{m}_i|}{S_i\rho_i}. \tag{31}$$

where $\Xi_i = [\frac{f_w}{Dhy_i}\Delta Z + \xi_i]$ is an overall axial loss coefficient, encompassing concentrated form losses ξ_i -resulting from the changing of the flow area due to the narrow connecting gap and frictional losses $\frac{f_w}{Dhy_i}\Delta Z$ due to fluid-rod interaction. $f_w = 4f$ is the Darcy friction factor, $Dhy_i = \frac{4S_i}{P_w}$ is the hydraulic diameter, and ξ_i the local form loss coefficient of subchannel i.

- Lateral direction friction term:

$$Friction_{ij} = -\frac{1}{2} g_{ij} \Delta Z \Xi_{ij} \rho |u_{ij}| u_{ij} = -\frac{1}{2} \Xi_{ij} \frac{w_{ij}|w_{ij}|}{S_{ij}\rho^{\star}}. \tag{32}$$

where Ξ_{ij} is an overall loss coefficient, encompassing lateral concentrated form and friction losses, and ρ^* is the donor cell density.

- Friction factor:

Friction factors are defined as a function of the flow regime. For square latices, a standard flow-dependent friction coefficient formulation is used in the KIT report [14]. This one reads as follows.

$$f_w \rightarrow \begin{cases} \frac{1}{64} & Re < 1 \\ \frac{64}{Re} & 1 \leq Re < 5^3 \\ 0.316 Re^{-0.25} & 5^3 \leq Re < 3^4 \\ 0.184 Re^{-0.20} & 3^4 \leq Re \end{cases} \tag{33}$$

The approach for triangular lattices is more complex. We follow the formulations used in the Chen and Cheng-Todreas models [15–17]. First, modeling the flow regime as a function of the ratio of pitch over diameter (P/D) for laminar and turbulent flow as follows:

$$Re_L = 320 \times 10^{\frac{P}{D}-1}, \tag{34}$$

$$Re_T = 10,000 \times 10^{0.7(\frac{P}{D}-1)}, \tag{35}$$

where Re_L is the critical Reynolds number for laminar flow and Re_T is the critical Reynolds number for the turbulent flow. In between the two, we obtain a transition regime.

Friction factors for the laminar, turbulent, and transition flow regimes in channel with bare

Flow Regime	Subchannel	$1.0 < \mathrm{P/D} < 1.1$			$1.1 < \mathrm{P/D} < 1.5$		
		a	b_1	b_2	A	b_1	b_2
Laminar	Interior	26.00	888.2	-3334	62.97	216.9	-190.2
	Edge	26.18	554.5	-1480	44.40	256.7	-267.6
	Corner	26.98	1636	-10050	87.26	38.59	-55.12
Turbulent	Interior	0.09378	1.398	-8.664	0.1458	0.03632	-0.03333
	Edge	0.09377	0.8732	-3.341	0.1430	0.04199	-0.04428
	Corner	0.1004	1.625	-11.85	0.1499	0.006706	-0.009567

Table 1: Coefficients for bare rod subchannel friction factor constants C'_{fi} in triangular grids.

rods are defined as follows:

$$f_{iL} = \frac{C_{fiL}}{Re_i}, \tag{36}$$

$$f_{iT} = \frac{C_{fiT}}{Re_i^{0.18}}, \tag{37}$$

$$f_{iTR} = f_{iL}(1-\psi)^{\gamma} + f_{iT}\psi^{\gamma}, \quad \psi = \frac{\log(Re) - \log(Re_L)}{\log(Re_T) - \log(Re_L)}, \gamma = \frac{1}{3}, \tag{38}$$

$$\tag{39}$$

where f_{iL}, f_{iT}, and f_{iTR} are the friction factors for laminar, turbulent, and transition flow regimes, respectively, and C_{fiL} and C_{fiT} are defined as a function of geometric factors and corresponding coefficients for the bare rod bundles. These latter ones are defined as follows:

$$C'_{f1} = a + b_1\left(\frac{P}{D} - 1\right) + b_2\left(\frac{P}{D} - 1\right)^2, \tag{40}$$

$$C'_{f2,3} = a + b_1\left(\frac{W}{D} - 1\right) + b_2\left(\frac{W}{D} - 1\right)^2, \tag{41}$$

$$\tag{42}$$

where the coefficients a, b_1, and b_2 are defined in Table 1. For edges and corners, $\frac{W}{D}$ is equal to $\frac{P}{D}$.

Similarly, for wire-wrapped rods, the resulting friction factors are defined as a function of geometry, wire angle, wire drag and sweeping constants, and bare rod friction coefficients

as follows:

$$f_1 = \frac{1}{Re_1^m}\left[C'_{f1}\left(\frac{P'_{w1}}{P_{w1}}\right) + W_d\left(\frac{3A_{r1}}{A'_1}\right)\left(\frac{De_1}{H}\right)\left(\frac{De_1}{D_w}\right)^m\right], \tag{43}$$

$$f_2 = \frac{C'_{f2}}{Re_2^m}\left[1 + W_s\left(\frac{A_{r2}}{A'_2}\right)\tan^2(\theta)\right]^{\frac{3-m}{2}}, \tag{44}$$

$$f_3 = \frac{C'_{f3}}{Re_3^m}\left[1 + W_s\left(\frac{A_{r3}}{A'_3}\right)\tan^2(\theta)\right]^{\frac{3-m}{2}}, \tag{45}$$

where m is fitted to the specific geometry while the W_d and W_s are the wire drag and sweeping coefficients, respectively, defined according to the flow regimes as follows:

$$W_{dT} = \left[19.56 + 98.71\left(\frac{D_w}{D}\right) + 303.47\left(\frac{D_w}{D}\right)^2\right]\left(\frac{H}{D}\right)^{-0.541}, \tag{46}$$

$$W_{dL} = 1.4W_{dT}\,, \tag{47}$$

$$W_{sT} = -11.0\log\left(\frac{H}{D}\right) + 19.0\,, \tag{48}$$

$$W_{sL} = W_{sT}\,. \tag{49}$$

$$\tag{50}$$

- Turbulent momentum transfer:

  The same model is used for bare square and triangular assemblies, which reads as follows:

$$Drag_{ij} = -C_T\sum_j w'_{ij}\Delta U_{ij} = -C_T\sum_j w'_{ij}\left[\frac{\dot{m}_i}{\rho_i S_i} - \frac{\dot{m}_j}{\rho_j S_j}\right]. \tag{51}$$

  where C_T is a turbulent modeling parameter, which is calibrated for bare assemblies. Specific models for wire-wrapped assemblies will be included as they become available.

- Turbulent enthalpy transfer: The same model is used for wire-wrapped and non-wire-wrapped assemblies since this term models the enthalpy transfer by the mixing cross flows. This one reads as follows:

$$h'_{ij} = \sum_j w'_{ij}\Delta h_{ij} = \sum_j w'_{ij}\left[h_i - h_j\right]. \tag{52}$$

- Turbulent cross flow:

  Different models are used for bare and wire-wrapped assemblies. In both case, the shape of the model is:

$$w'_{ij} = \beta S_{ij} \bar{G}, \quad \frac{dw'_{ij}}{dz} = \frac{w'_{ij}}{\Delta Z} = \beta g_{ij} \bar{G}. \tag{53}$$

  where β is the turbulent mixing parameter or thermal diffusion coefficient, and $\bar{G}$ is the average mass flux of the adjacent subchannels. The β term is a tuning parameter for the mixing model. Physically, it is a non-dimensional coefficient that represents the ratio of the lateral mass flux due to mixing to the axial mass flux. In a single-phase flow, no net mass exchange occurs, both momentum and energy are exchanged between subchannels, and their rates of exchange are characterized in terms of hypothetical turbulent interchange flow rates ($w_{ij}^{'H}, w_{ij}^{'M}$) [1], respectively. Simplifying for a single-phase flow, we have made the approximation that the rate of turbulent exchange for energy and momentum are equal:

$$w'_{ij} = w_{ij}^{'H} = w_{ij}^{'M}. \tag{54}$$

  For bare assemblies, the coefficient β is typically between 0.05 and 0.15 [15] and is calibrated for specific geometries. For wire-wrapped assemblies, according to the Cheng-Todreas model [15], turbulent mixing is modeled separately for inner and peripheral subchannels as a function of geometry and wire angle. Turbulent mixing coefficients for the inner subchannels are given as follows:

$$\beta = C_m \left(\frac{A_{r1}}{A_1} \right)^{0.5} \tan(\theta), \tag{55}$$

  and sweeping in the corners and edge subchannels (equivalent to mixing in the inner subchannels) is given by

$$\beta = C_s \left(\frac{A_{r2}}{A_2} \right)^{0.5} \tan(\theta), \tag{56}$$

  where the C_m and C_s coefficients are dependent on the flow regime and are defined as follows

for laminar and turbulent regimes:

$$C_{mL} = 0.077 \left(\frac{P-D}{D} \right)^{-0.5}, \quad C_{sL} = 0.033 \left(\frac{H}{D} \right)^{0.3}, \tag{57}$$

$$C_{mT} = 0.14 \left(\frac{P-D}{D} \right)^{-0.5}, \quad C_{sT} = 0.75 \left(\frac{H}{D} \right)^{0.3}, \tag{58}$$

For transition flows, we used a log-blending model that is defined as follows:

$$C_{sTR} = C_{sT} + (C_{sT} - C_{sL})\psi^{\gamma}, \tag{59}$$

$$C_{mTR} = C_{mT} + (C_{mT} - C_{mL})\psi^{\gamma}, \tag{60}$$

$$\psi = \frac{\log(Re) - \log(Re_L)}{\log(Re_T) - \log(Re_L)}, \gamma = \frac{2}{3}. \tag{61}$$

- Radial conduction factor:

  The radial conduction factor is defined after the Cheng-Todreas model as follows [17]:

$$\eta_{ij} = \eta = 0.66 \left(\frac{P_{ij}}{D_i} \right) \left(\frac{S_{ij}}{D_i} \right)^{-0.3} \tag{62}$$

- Equation of state:

  The set of equations is augmented by fluid property relationships.

  - Temperature as a function of pressure and enthalpy: $T = T(P, h)$.
  - Density as a function of temperature and pressure: $\rho = \rho(T, P)$.
  - Dynamic viscosity as a function of temperature and pressure: $\mu = \mu(T, P)$

3.1.5 Algorithm

To implement a single-phase subchannel code within MOOSE, we developed a hybrid numerical method for solving the subchannel equations. The core of this method is the subdivision of the fuel assembly into axial blocks, as shown in Figure 2.

When discretizing the subchannel equations, one subdivides the fuel assembly axially into N axial cells. If the flow is mainly one dimensional, such as in standard LMFRs operation conditions,

one may solve one axial level at a time before solving the axial level above. This gives rise to the commonly implemented *marching* scheme in subchannel codes [2, 18] as one "marches" from the bottom to the top of the assembly while solving. The advantage of this sweeping-type discretization scheme is that one can achieve a high-speed solution of the subchannel system as only small systems are obtained per level. However, this scheme is ineffective if recirculating flow phenomena is present in the assembly. Hence, another choice would be to solve all equations at the same time for the N axial cells. However, in this case, one would obtain a very large system that may significantly deteriorate the numerical performance. The hybrid scheme proposed in this work allows us to divide the assembly into NB blocks of $NC \leq N$ axial cells, as shown in Figure 2, note that $NB \times K = N$. In each of these blocks, we developed a monolithic solve for the subchannel equations. The solution stencil for each block is provided in Figure 3. Blocks are solved from bottom to top as in the marching scheme. Note that, if we have $NC = 1$ and $NB = N$, we obtain the standard, fast-running marching solve. On the other extreme, if $NC = N$ and $NB = 1$, we obtain a monolithic solve for the whole assembly. In between, we obtain relatively fast-running schemes able to deal with recirculation problems within the block extent. The parameters NB and N are defined by the user in the input file. Then, NC is automatically computed, adapting the number of cells in the last block so that the total number of solved cells matches N.

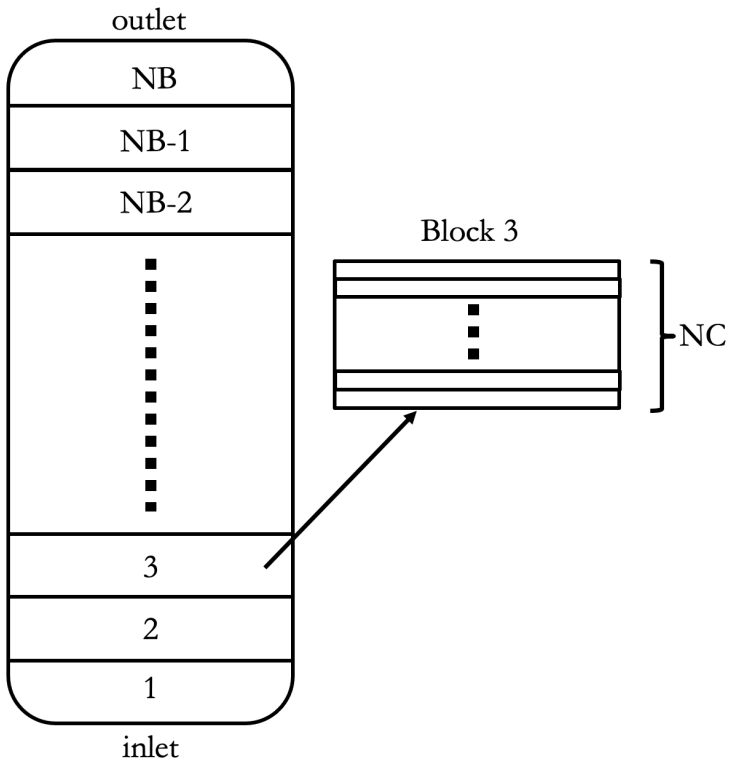

Figure 2: Division of the subchannel assembly into blocks [3].

The solution scheme within each block is presented in Figure 3. The core of the block solver is to construct a combined residual function based on the lateral momentum equation, Equation (66). To solve this equation, we use the JFNKM. The key solver of the PrSub code is PETSc's Scalable Nonlinear Equations Solvers (SNES) found in [19]. The SNES class includes methods for solving systems of nonlinear equations in the form: **F (x)** $= 0$. PETSc's default method for solving the nonlinear equation is Newton's method. The general form of the n-dimensional Newton's method becomes:

$$\boldsymbol{x_{k+1}} = \boldsymbol{x_k} - \boldsymbol{\mathcal{J}}(\boldsymbol{x_k})^{-1}\boldsymbol{F}(\boldsymbol{x_k}), \quad k = 0, 1, .., \tag{63}$$

In practice, the Newton iteration (63) is implemented by the following two steps:

$$\text{1. Approximately solve } \boldsymbol{\mathcal{J}}(\boldsymbol{x_k})\Delta\boldsymbol{x_k} = -\boldsymbol{F}(\boldsymbol{x_k}) \tag{64}$$

$$\text{2. Update } \boldsymbol{x_{k+1}} = \boldsymbol{x_k} + \Delta \boldsymbol{x_k} \tag{65}$$

A JFNKM uses a Krylov method to solve the linear system (64) that appears in each Newton step. Key to a Newton-type solver is the formation of the Jacobian matrix $\mathcal{J}$. It is usually difficult to compute the exact Jacobian, so we prefer to use a method that only requires an approximation of the Jacobian. One such approximate comes from a "Picard linearization," which writes the nonlinear system as: $\boldsymbol{F}(\boldsymbol{x}) = \boldsymbol{A}(\boldsymbol{x})\boldsymbol{x} - \boldsymbol{b}$, where $\boldsymbol{A}(\boldsymbol{x})$ usually contains the lower-derivative parts of the equation. The Picard iterative procedure can be performed by defining $\boldsymbol{\mathcal{J}}(\boldsymbol{x})$ to be $\boldsymbol{A}(\boldsymbol{x})$. Sometimes this iteration exhibits better global convergence than the Newton linearization. In a method, such as the one we use here, we do not calculate the Jacobian; rather, we approximate the action of the Jacobian on a vector: $\boldsymbol{\mathcal{J}}(\boldsymbol{u})\boldsymbol{\alpha} \approx \frac{\boldsymbol{F}(\boldsymbol{u}+h*\boldsymbol{\alpha})-\boldsymbol{F}(\boldsymbol{u})}{h}$ The core of our solution method is noting that if the cross flows w_{ij} are known, then the axial fluxes and pressure drop are directly defined by (3) and (4). Hence, we built a residual function for the nonlinear solve directly on the cross fluxes as follows:

$$f(w_{ij}) = \frac{\partial w_{ij}}{\partial t} L_{ij} + \frac{L_{ij}}{\Delta z} \Delta(w_{ij} \bar{U}_{ij}(w_{ij})) - S_{ij} \Delta P_{ij}(w_{ij}) + \frac{1}{2} K_{ij} \frac{w_{ij}|w_{ij}|}{\rho^*}. \tag{66}$$

The main unknown variable in this nonlinear residual is the cross flow w_{ij}. The combined residual function we created calculates the nonlinear residual $f(w_{ij})$ after it updates the other main flow variables, such as mass flow $\dot{m}_i$, turbulent cross flow w'_{ij}, pressure drop ΔP_i, and pressure P_i through Equations (3), (4), and (53), using the current w_{ij} as needed. So every time this function is used by the Newton solver, the flow variables are updated. This means that, as we solve the lateral momentum equation, we are solving for all the flow variables at the same time. Similarly, as in COBRA [2], the variable P_i is the local pressure minus the exit pressure, $P_i(z) - P_{exit}$, so at the exit, P_i is zero.

Once the main flow variables converge in a block, we solve the enthalpy conservation equation, Equation (6) and retrieve enthalpy (h) in all block nodes. In the case where no heat is added to the fluid, the enthalpy does not need to be calculated unless we have a nonuniform enthalpy inlet distribution. Using enthalpy, pressure, and the equations of state, we can calculate the temperature T_i and fluid properties, such as density ρ_i and viscosity μ_i. After we update the

fluid properties, the procedure is repeated until the temperature solution has converged. Once the temperature solution converges, we move on to the next block. Once the temperature solution converges in all blocks, we check if pressure has converged in all blocks. If not, we repeat the procedure starting again from the first block until pressure has converged.

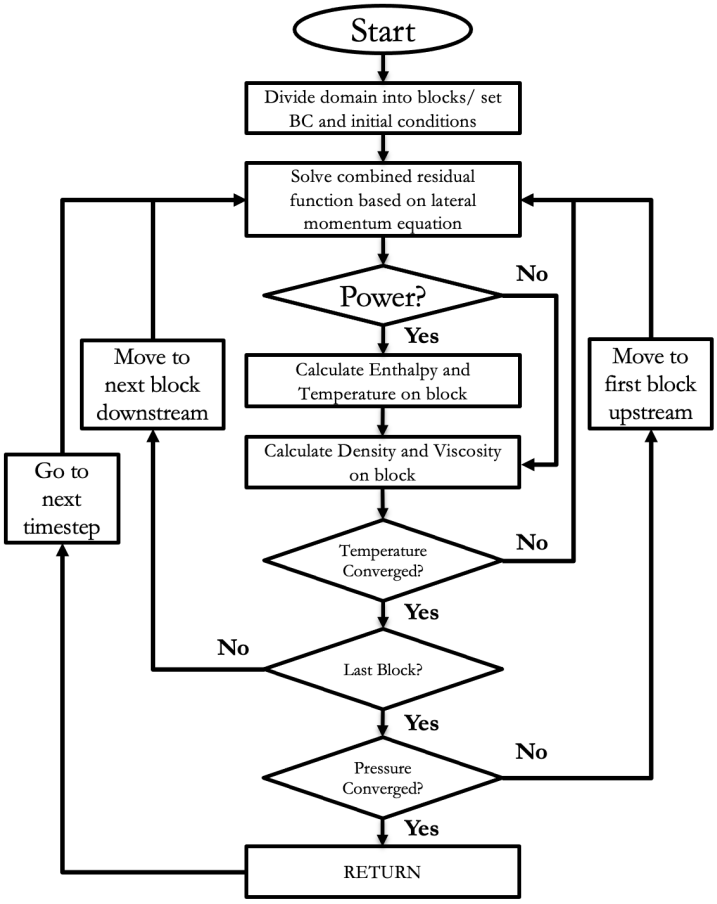

Figure 3: Subchannel hybrid numerical scheme [3].

3.1.6 Subchannel Integration into MOOSE

The PrSub code was implemented using the *ExternalProblem* class in MOOSE [20]. Developing a subchannel application within MOOSE posed a unique challenge. This is because MOOSE works on minimizing a residual of partial differential equations at the quadrature points of a finite element mesh. This mode of operation is significantly different from the standard subchannel approach that is first based on a FVM-type discretization and second uses specifically tailored discretization and solution algorithms. Specifically, it was impossible to use the FEM problem

context provided in MOOSE to solve the subchannel equations. However, we opted to inherit from and extend MOOSE's FEM mesh class. In this way, PrSub can easily be coupled to other MOOSE-based applications by using the multi-app system to organize MOOSE FEM, FVM, and PrSub instances and transfer information between them using multi-app transfers.

ExternalProblem is an intermediate class used as an extension point (inheritance) for externally coupled codes (MOOSE-wrapped apps). To achieve the external coupling, this interface overrides the "solve" method along with a method for testing iteration convergence. The *ExternalProblem* object contains the extra interface function necessary for creating and maintaining current solution information on an "external" mesh object. Specifically, the *ExternalProblem* creates a final override for the solve() method that triggers three different callbacks: syncSolutions (Direction::TO_EXTERNAL_APP); externalSolve(); and syncSolutions (Direction::FROM_EXTERNAL_APP).

PrSub is not based on the FEM-based solver that uses the FEM problem context to link discretization and solver layers. Therefore, the variables that PrSub solves for cannot be defined as nonlinear variables but must be stored as auxiliary variables that are in turn set by the PrSub solver.

In order for MOOSE to understand which variables should be maintained on the ExternalMesh, another *Action* was created that is called during the problem setup to assist in adding the necessary AuxVariables to the simulation.

3.2 Porous Media Approach to LMFR

The flow within the fuel and control rod elements of LMFRs can be modeled using a porous media model. In a porous media model, the fuel or control rods and fluid occupy the same space. The fluid volume fraction is referred to as the porosity of the shared volume. Balance equations for fluid mass, momentum, energy, and solid energy are coupled via momentum and energy exchanges described by correlations. One advantage of this approach is the ability to seamlessly couple porous flow regions to free-flow regions outside of the immediate core regions without changing the modeling paradigm. The porous media approach has been used by GeN-Foam [21] and Star-CCM+ [5] to model sodium fast reactors (SFRs). In this work, we closely follow the approach of Reference [5] but use *Pronghorn* instead of Star-CCM+.

The porous flow equations for incompressible flow are given by:

$$\begin{aligned}
\nabla \cdot \vec{v} &= 0 \\
\frac{\partial \vec{v}}{\partial t} + \nabla \cdot \left(\gamma^{-1}\vec{v} \otimes \vec{v}\right) &= -\frac{\gamma}{\rho}\nabla p + \gamma \vec{g} - W\vec{v}_I \\
\gamma\rho\frac{\partial e}{\partial t} + \rho\nabla \cdot (h\vec{v}) - \nabla \cdot \left(\kappa_f \nabla T\right) + \alpha(T - T_s) &= 0 \\
(1-\gamma)\rho_s c_{p,s}\frac{\partial T_s}{\partial t} - \nabla \cdot (\kappa_s \nabla T_s) - \alpha(T - T_s) &= \dot{q}''' \text{ on } \Omega_f,
\end{aligned} \tag{67}$$

where $\vec{v}$ is the superficial velocity defined as $\vec{v} = \gamma\vec{v}_I$, with γ as the porosity and $\vec{v}_I$ as the interstitial or physical velocity, ρ is the constant density, p is the pressure, e is the internal energy, h is the enthalpy, T is the fluid temperature, T_s is the solid temperature, ρ_s is the solid density, $c_{p,s}$ is the specific heat of the solid phase, $\vec{g}$ is the gravity vector, W is the pressure drop coefficient, κ_f is the effective thermal conductivity of the fluid, α is the volumetric heat transfer coefficient between the fluid and the solid phase, κ_s is the effective solid thermal conductivity, and $\dot{q}'''$ is the heat source in the solid (e.g., fission heat source). The effective thermal conductivities κ_f and κ_s are in general diagonal tensors. The fluid domain Ω_f comprises porous regions with $0 < \gamma < 1$ and free flow regions with $\gamma = 1$; in the free-flow region, T_s is not solved, $\alpha = 0$, $W = 0$, and $\kappa_f = k_f$ (where k_f is the thermal conductivity of the fluid). The assumption of an incompressible flow is not a limitation of Pronghorn, as Pronghorn provides a weakly compressible flow formulation [22].

The ducts are modeled as a solid using the equation:

$$\rho_s c_{p,s}\frac{\partial T_s}{\partial t} - \nabla \cdot (k_s \nabla T_s) = 0 \text{ on } \Omega_s, \tag{68}$$

where k_s is the standard thermal conductivity of the duct material.

Eq. 67 is augmented by the following boundary conditions:

- The flow variables p and $\vec{v}$ use specified velocity inlet, specified pressure outlet, and slip wall boundary conditions.
- The fluid energy equation has fixed temperature inflow conditions and adiabatic walls.

- Robin boundary conditions are applied on the boundaries between Ω_f and Ω_s:

$$-k_s \vec{n} \nabla T_s|_{\Omega_s} - h\left(T_s|_{\Omega_s} - T|_{\Omega_f}\right) = 0, \tag{69}$$

  where h is the areal heat transfer coefficient between fluid and wrapper.

The following correlations are used to compute W, κ_f, κ_s, κ_f, and α.

- For all correlations, the Reynolds number is defined as:

$$Re = \frac{D_h \rho \|\vec{u}_I\|}{\mu}, \tag{70}$$

  where D_h is the hydraulic diameter of the fuel element, the Prandtl number is denoted by Pr, and the Peclet number is denoted by Pe.

- The Rehme drag coefficient [23] is used to compute the drag coefficient in all rodded regions and is a diagonal tensor given by:

$$W = \begin{bmatrix} 100w & 0 & 0 \\ 0 & 100w & 0 \\ 0 & 0 & w \end{bmatrix}, \tag{71}$$

  where we assume the control and fuel rods are aligned with the z-direction and the modification of the drag coefficients in the x-y plane is taken from Reference [5]. The value of w is computed by:

$$w = \gamma f' F \frac{S_b}{S_t} \frac{\|\vec{v}_I\|}{2D_h}, \tag{72}$$

  where S_t is the total wetted perimeter and S_b is the wetted perimeter of the bundle and wire wrap. f' is defined by:

$$f' = \frac{64}{Re'} + \frac{0.0816}{Re'^{0.133}} \quad , \tag{73}$$

  where Re' is the modified Reynolds number defined by:

$$Re' = Re\sqrt{F}. \tag{74}$$

F is defined by:

$$F = \sqrt{\frac{P}{D_r}} + \left[7.6 \frac{D_r + D_w}{H} \left(\frac{P}{D_r} \right)^2 \right]^{2.16}, \tag{75}$$

where P is the pitch of the fuel and control rods, D_r is the rod diameter, D_w is the wire wrap diameter, and H is the wire wrap pitch.

- The effective thermal conductivity κ_f is identical to the thermal conductivity of the fluid except in the rodded flow regions:

$$\kappa_f = \begin{bmatrix} \gamma k_f & 0 & 0 \\ 0 & \gamma k_f & 0 \\ 0 & 0 & \gamma k_f \end{bmatrix} \tag{76}$$

  In the rodded core region, thermal dispersion leads to an enhanced exchange of heat in the fluid orthogonal to the main flow direction and a reduction in the main flow direction. We account for these changes using the effective thermal conductivity in the rod bundles computed using the correlation provided in Reference [24]:

$$\kappa_f = \begin{bmatrix} \tilde{\kappa}_f & 0 & 0 \\ 0 & \tilde{\kappa}_f & 0 \\ 0 & 0 & \gamma k_f \end{bmatrix}, \tag{77}$$

  where:

$$\tilde{\kappa}_f = \left(1 - \frac{D_r}{P} \right) k_f + k_f Pe \left(0.85 - 12.8 \left| \frac{P}{D_r} - 1.25 \right|^{1.424} \right) \frac{D_r}{H}. \tag{78}$$

- The volumetric heat transfer coefficient α is computed using the approach in Reference [25]:

$$\alpha = (1 - \gamma) \frac{A_r}{V_r} \sqrt{\frac{v_{I,t}^2 + v_{I,a}^2}{\frac{v_{I,a}^2}{h_a^2} + \frac{v_{I,t}^2}{h_t^2}}}, \tag{79}$$

  where A_r is the surface area of the fuel pin, V_r is the volume of the fuel, the subscripts a and t indicate axial and transversal (i.e., $v_{I,a}$ is the velocity in along the duct direction, while $v_{I,t}$ is the velocity in the plane orthogonal to the duct direction), and h_a and h_t are axial

and transversal heat transfer coefficients, respectively. The axial heat transfer coefficient is computed using the correlation in Reference [26]:

$$h_a = 0.047 \frac{k_f}{D_h} \left[1 - e^{-3.8(P/D_r - 1)}\right] \left(Pe^{0.77} + 250\right). \tag{80}$$

The transversal heat transfer coefficient is computed using the correlation in Reference [27]:

$$h_t = 0.958 \frac{k_f}{D_h} \left(\frac{\phi_1}{D_r}\right)^{0.5} Pe^{0.5}, \tag{81}$$

where:

$$\frac{\phi_1}{D_r} = 13.5970 \left(\frac{P}{D_r}\right)^4 - 92.6810 \left(\frac{P}{D_r}\right)^3 + 237.1231 \left(\frac{P}{D_r}\right)^2 - 271.0070 \frac{P}{D_r} + 119.8956. \tag{82}$$

- The wall heat transfer coefficient h is computed using the Lyon-Martinelli correlation [28]:

$$h = \frac{k_f}{D_h} \left(4 + 0.025 Pe^{0.8}\right) \tag{83}$$

The hexagonal fuel elements are meshed using MOOSE's reactor module [29]. We use two different approaches in this work:

- A higher fidelity approach using the two-region porosity model of Reference [5] and explicitly modeling the inter-wrapper space as a flow region
- A lower fidelity approach using the one-region porosity model of Reference [5] and treating the wrapper and inter-wrapper space as a single no-flow region with effective thermal properties. This approach is not recommended for future modeling efforts, but the MOOSE thermal-hydraulics solver is currently based on a Newton approach with a direct linear solve (*LU*), which becomes computationally expensive in three-dimensional geometries.

The meshes for the higher and lower fidelity approaches are depicted in Figure 4.

LMFR fuel elements have orifices at the inlets to ensure a flow distribution that reduces the disparity in fuel element outlet temperatures. This is modeled by a distributed pressure drop over the orifice region. If the orifice has a thickness of Δz and a loss coefficient of C, the corresponding

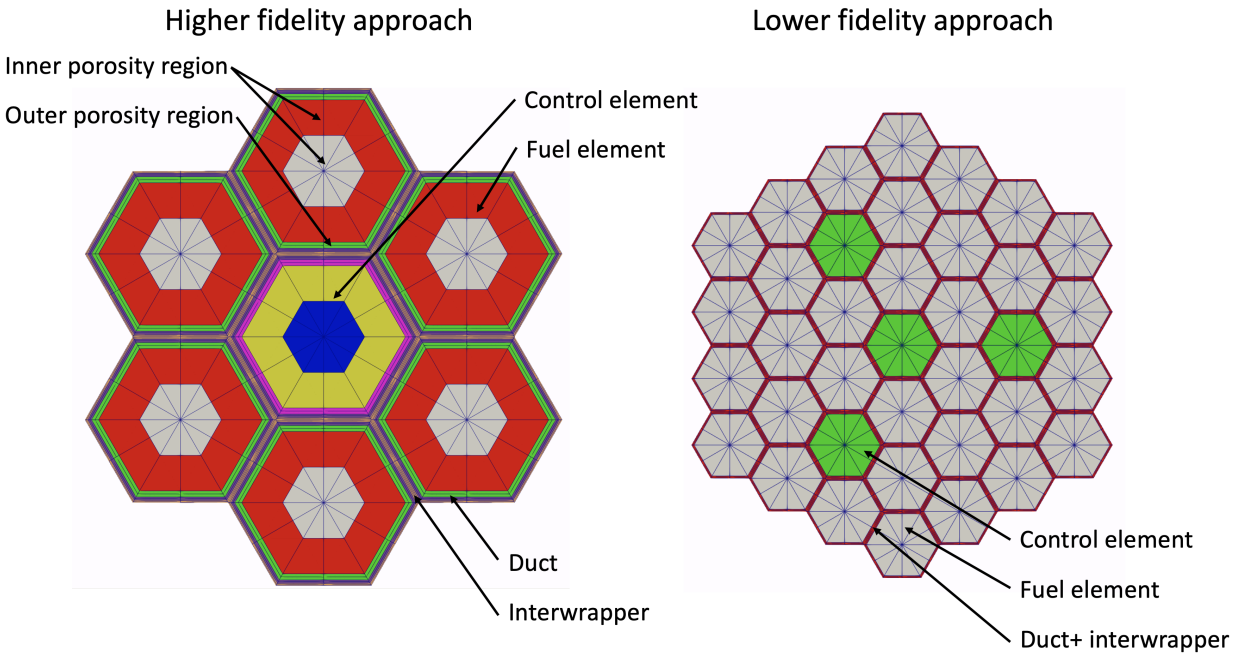

Figure 4: The mesh for the higher and lower fidelity approach for modeling hexagonal fuel element LMFR cores using the porous media approximation. The different fuel element types are indicated as well as different regions in each fuel assembly.

W is given by:

$$W = \frac{\gamma C}{2\Delta z}\|\vec{v}_I\|. \tag{84}$$

In practice, the orifice loss coefficient might be calibrated to measure the flow distribution at representative reactor flow conditions.

Modeling control elements often poses more challenges. First, partially withdrawn control elements create additional irreversible pressure drops at the control rod tips. Second, some control elements feature more complicated geometries (e.g., double-ducted control assemblies [30]). Both cases are modeled using the distributed loss coefficient defined in Equation 84.

The simplest approach to modeling the pressure drop in a single-ducted control element at the control rod tip is to use a loss coefficient for a sudden reduction in flow area. The pressure drop at a sudden reduction in flow area is given by References [31, 32]:

$$\Delta p = \frac{\rho}{2}\|\vec{v}_{I,o}\|^2 \frac{1}{2}\left(1 - \frac{A_o}{A_i}\right), \tag{85}$$

where $\vec{v}_{I,o}$ is the interstitial velocity at the outlet of the sudden flow area reduction geometry, A_i

is the inlet flow area, and $A_o < A_i$ is the outlet flow area. The pressure drop correlation can be generalized to where the flow areas are described by porosities and rewritten in terms of the superficial velocity:

$$\Delta p = \frac{\rho}{2} \|\vec{v}\|^2 \frac{1}{2\gamma_o^2} \left(1 - \frac{\gamma_o}{\gamma_i}\right), \tag{86}$$

The corresponding drag coefficient W for a porous layer of thickness Δz is given by:

$$W = \frac{\gamma^3}{2\Delta z} \|\vec{v}_I\| \frac{1}{2\gamma_o^2} \left(1 - \frac{\gamma_o}{\gamma_i}\right). \tag{87}$$

Note, there is a difference between γ_i and γ_o on the one hand and γ on the other. γ_i and γ_o are the fixed porosities before and after the flow area reduction, respectively, while γ is the spatially dependent porosity in the element that the drag term is applied to. This distinction allows researchers to apply the drag from a flow area reduction either before or after the flow area reduction takes place. In addition, this formulation immediately accounts for the porosity smoothing that Pronghorn allows users to enable. In the future, an interface kernel might be used to model concentrated pressure drops.

For modeling more complicated configurations (e.g., double-ducted assemblies), we used a loss coefficient that differs across the duct (i.e., orthogonal to the main flow direction). The loss coefficient should be adjusted to reproduce the flow split between the inner and outer portions of the double-ducted fuel element and the overall pressure drop. The loss coefficient will highly depend on the geometry and will have to be calibrated to experiments or cfd simulations.

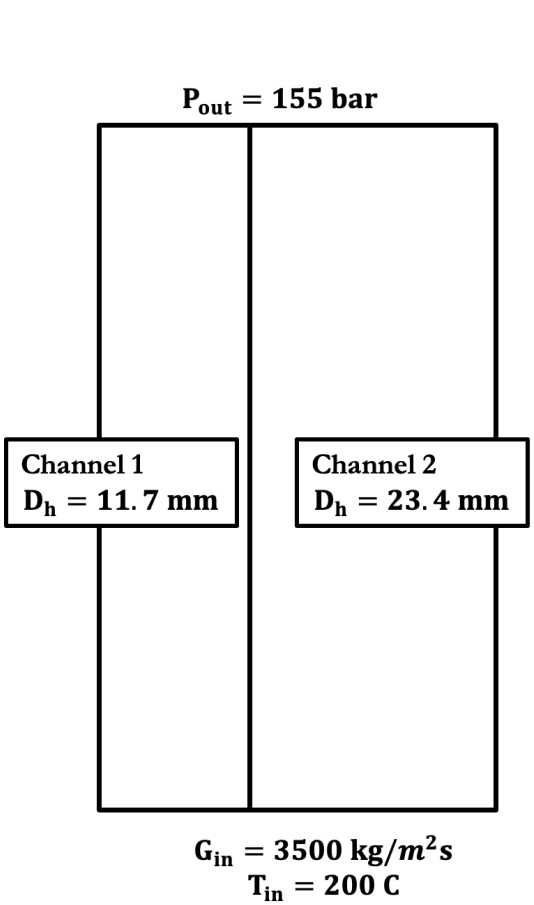

(a) Friction model verification.

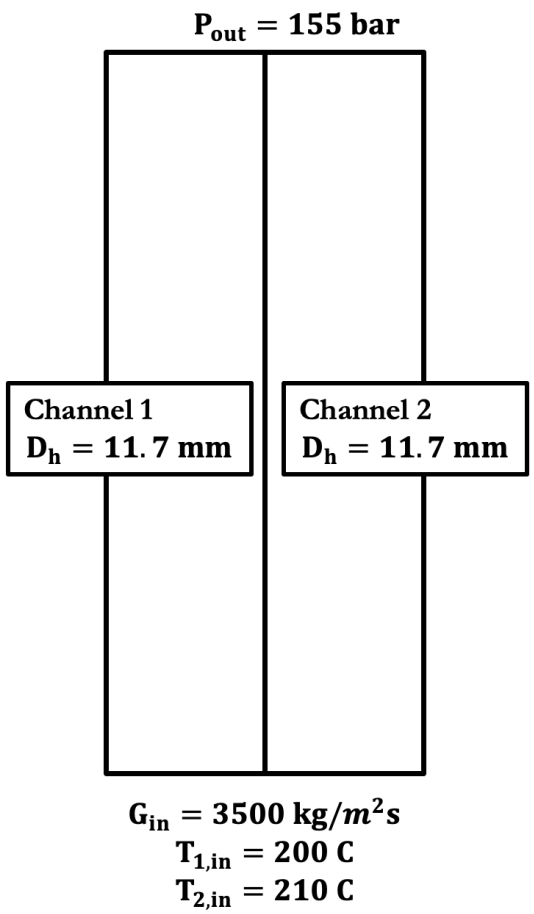

(b) Enthalpy mixing model verification.

Figure 5: Verification problems [3]. (**a**) Two-channel problem for friction model verification. (**b**) Two-channel problem for enthalpy mixing model verification.

4. Verification of the Subchannel Implementation

In this section, we present the verification of the friction and turbulent mixing models. We have already published some of this verification code in [3]. However, we are included this results here for completeness. The problems we've discussed were chosen because they isolate the specific physics in question and are the same problems used in the Cobra-TF (CTF) void-drift validation study [33].

4.1 Two-Channel Friction Model Verification

In this case, we have sought to study a problem where the effects of friction are clearly discernible. We know that crossflow in the single-phase case is driven by a lateral pressure

gradient and turbulence. By deactivating turbulence in our test model case, crossflow can only be the result of a lateral pressure imbalance, which for a model with no form losses (spacer grids), can only be driven by unequal frictional losses. Friction loss depends on the hydraulic diameter, so it makes sense to devise a two-channel problem using channels with an unequal flow area.

Channel-2 has twice the hydraulic diameter of Channel-1. We set the model length to 10 m to allow the flow to fully develop. A sketch of the two-channel problem is shown in Figure 5a. The different frictional pressure drops create a lateral pressure gradient that drives flow from the small channel to the large channel. Moving up the channels, velocity decreases in Channel-1, which decreases the frictional pressure drop. At the same time, velocity grows larger in Channel-2, which increases the frictional pressure drop. This continues until the frictional pressure drop is the same in both channels, at which point crossflow between the two channels ceases. At this point, the channels are in mechanical equilibrium. An analytical expression is derived for the flow distribution at the point of mechanical equilibrium.

$$\dot{m}_{in} = \dot{m}_2 \left(1 + \left(\frac{D_{h,2}}{D_{h,1}} \right)^{\frac{C_2 - 1}{C_2 + 2}} \frac{A_1}{A_2} \right). \tag{88}$$

where m_{in} is the mass flow at the inlet, m_1, m_2 are the mass flows of the two channels at equilibrium, $D_{h,2}, D_{h,1}$ the hydraulic diameters, A_1, A_2 the flow surface areas, and C_2 is a friction modeling parameter when we define the friction factor, $f = C_1 Re^{C_2}$, as a function of the Reynolds number. We can compare the analytical prediction with the code results in Figure 6a. The code converges to the analytical prediction.

4.2 Turbulent Mixing Verification

In this case, we wanted to study a problem where the effects of turbulence are clearly discernible. Turbulence causes both momentum and enthalpy mixing through the terms:

$$Drag_{ij} = -C_T \sum_j w'_{ij} \Delta U_{ij}, \tag{89}$$

$$h'_{ij} = \sum_j w'_{ij} \Delta h_{ij}. \tag{90}$$

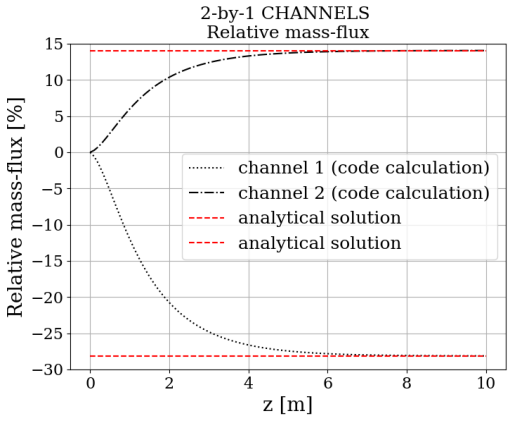

(a) Friction model verification results.

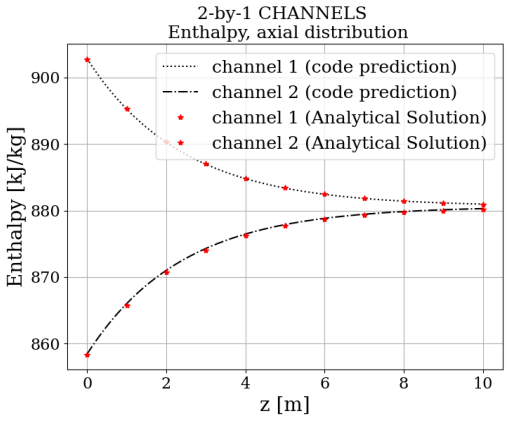

(b) Enthalpy mixing model verification results.

Figure 6: Verification problems. (**a**) Two-channel problem for friction model verification. (**b**) Two-channel problem for enthalpy mixing model verification.

Because the models for turbulent mixing are gradient-driven based on $\Delta h, \Delta U$, it is necessary to make a gradient in either enthalpy or velocity to observe the effects of turbulence. It is easier to focus on the energy equation and deactivate the density calculation. The problem geometry consists of two identical channels connected by a gap, as shown in Figure 5b. To test the turbulent mixing model, the inlet temperature of one channel is raised by 10°C. Turbulent enthalpy mixing will transfer heat from the one channel to the other. The solution given by the code is then compared to the analytical solution.

$$h_1 = \frac{(h_{1,in} + h_{2,in})}{2} - \frac{1}{2}(h_{2,in} - h_{1,in}) \exp\left(-\frac{2\frac{dw'_{12}}{dz}}{\dot{m}} z\right) \tag{91}$$

$$h_2 = \frac{(h_{1,in} + h_{2,in})}{2} + \frac{1}{2}(h_{2,in} - h_{1,in}) \exp\left(-\frac{2\frac{dw'_{12}}{dz}}{\dot{m}} z\right) \tag{92}$$

where $h_{1,in}, h_{2,in}$ are the enthalpies at the inlet of the two channels and $\frac{w'_{12}}{z}$ is the turbulent crossflow between the two channels per unit length. We see that the code prediction and analytical solution are in good agreement in Figure 6b. We calculated the maximum absolute error as $Error_{max} = 2.45 \times 10^{-1}$kJ/kg and the maximum relative error as $Error_{relative,max} = 2.81 \times 10^{-4}$.

5. Validation of the subchannel implementation

The validation data for subchannel codes for flow of sodium in hexagonal assemblies is scarce when compared to the data available for liquid water. This paper presents the validation of two widely used test cases in this section: (i) validation on the fuel failure mockup (FFM) experiment at ORNL (called ORNL's 19-pin benchmark henceforward) and (ii) validation on Toshiba's 39-pin benchmark. Moreover, multiple validation cases have been performed for light-water reactors, which allows us to increase the validation base of the current solution strategies.

5.1 ORNL's 19-Pin Benchmark

The FFM experiment was built at ORNL for studying the thermal-hydraulic flow characteristics in SFR assemblies [34]. We will use the results of Test Series 2 for validation. In this series, the fuel rods of the FFM experiment were heated by 19 identical electric cartridges. The configuration and external heat fluxes of this cartridge matches typical values expected for SFRs. The measurements in Test Series 2 focused on the distribution of temperatures at the exit of the fuel assembly, the duct walls, and the rod bundle. The nature of the heat source and lack of neighboring assemblies make the distribution of temperatures at the rod bundle and duct atypical for LMFRs. Therefore, this data was deemed of secondary importance for validating PrSub for SFR applications. In contrast, the distribution of temperatures at the exit of the fuel assembly is indicative of coolant heating and flow mixing in the fuel bundle, which is expected to be representative of the one in an actual SFR. Therefore, we have focused our validation work in predicting the distribution of temperatures at the exit of the fuel assembly.

The design parameters for the Test Series 2 of the FFM experiment are presented in Table 2. Pressure is assumed to be constant at the assembly outlet and temperature and mass flux to be constant at its inlet. The fuel bundle is divided between inlet, heated, and outlet sections along the rod in increasing elevation. A nonzero linear heat rate is only assigned to the heated part of the rod, while no power is imposed at the inlet and outlet sections.

The numbering of rods and subchannels in the fuel assembly is presented in Figure 7. The left panel of this figure shows the rod position along with the assigned number, while the subchannel centers are indicated with red dots. On the right panel of this figure, the red dots indicate the

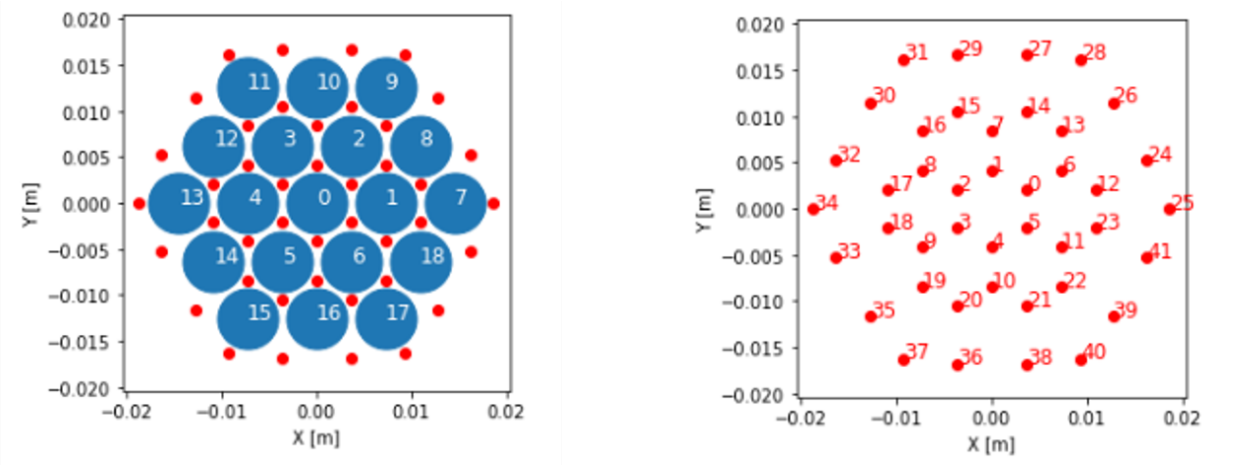

(a) Rod positions.

(b) Subchannel positions.

Figure 7: Rod and subchannel positions and numbering adopted for ORNL's 19-pin benchmark. (**a**) Position and numbering of the heated rods with the subchannel center indicated with red dots. (**b**) Center position and numbering of the subchannels.

centers of the subchannels, and it shows the numbering convention adopted for the subchannels. Due to hexagonal symmetry in the experiment, the temperature distribution has been measured over the subchannels that approximately lie on the diagonal line that connects opposed vertices in the duct. The orientation connects the south-west vertex to the north-east one. For our numbering convention, this line includes subchannels 37, 36, 20, 10, 4, 1, 14, and 28.

The key factor dominating the temperature profile in the domain outlet is the competing effect between heat convection and heat conduction in the coolant. An example of the axial and lateral mass flow rates and the temperature and viscosity fields obtained for a high-flow-rate configuration in ORNL's 19-pin benchmark is presented in Figure 8. The flow rapidly develops over the assembly. However, there is a significantly larger flow field in the outer gaps of the rod bundle. This results in the outer rods and channels being colder than the ones in the center. The temperature difference between outlet and inner subchannels increases with the increasing mass flow rate. There is a small competing effect due to the viscosity in the center of the channels being smaller due to heating, but this effect is of second order compared with the flow driven by the pressure drop effects. However, as mass flow decreases, heat conduction in the sodium coolant starts dominating over heat convection, and hence, the temperature profiles become flatter at the exit. In summary, the temperature distribution measured at the assembly outlet can be regulated by the balance between convection and conduction, which is experimentally regulated

by changing the axial mass flux and power at the rod bundles.

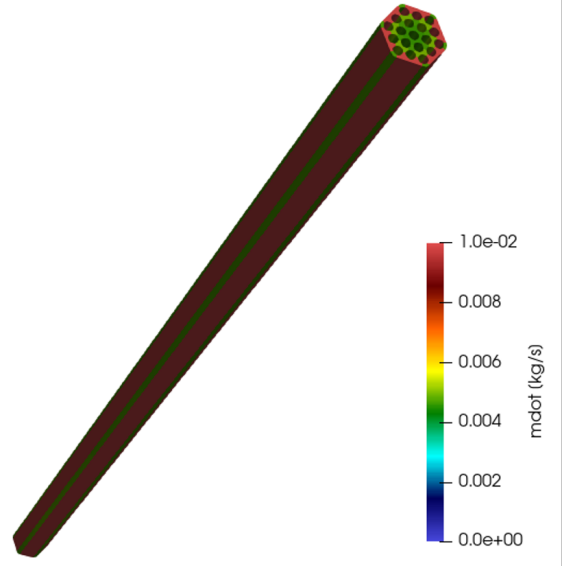

(a) Axial mass flow.

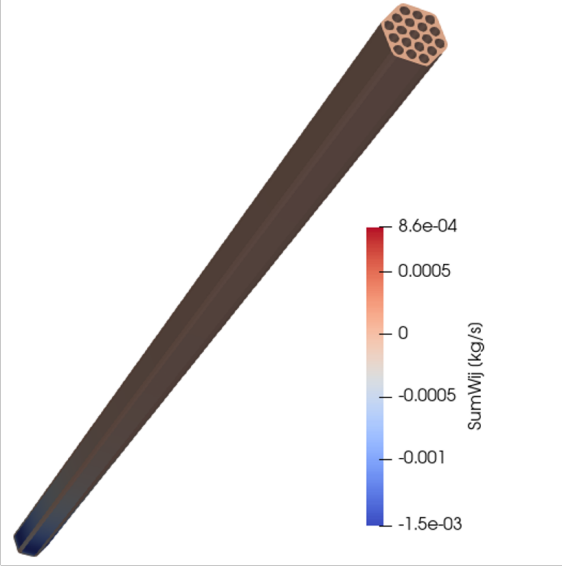

(b) Lateral mass flow.

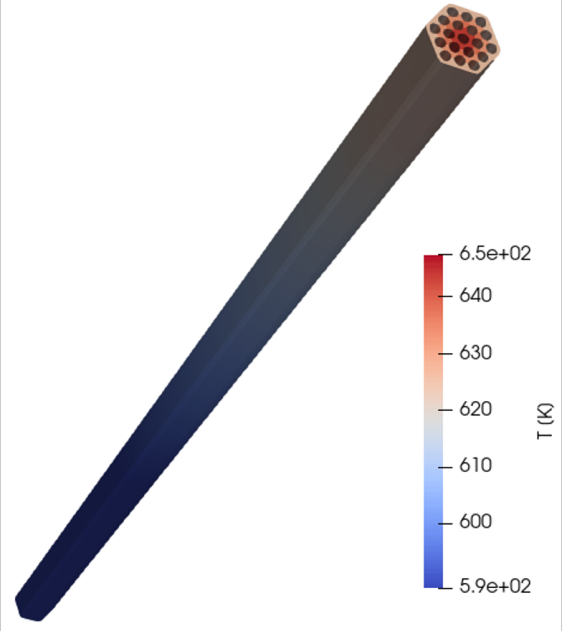

(c) Temperature.

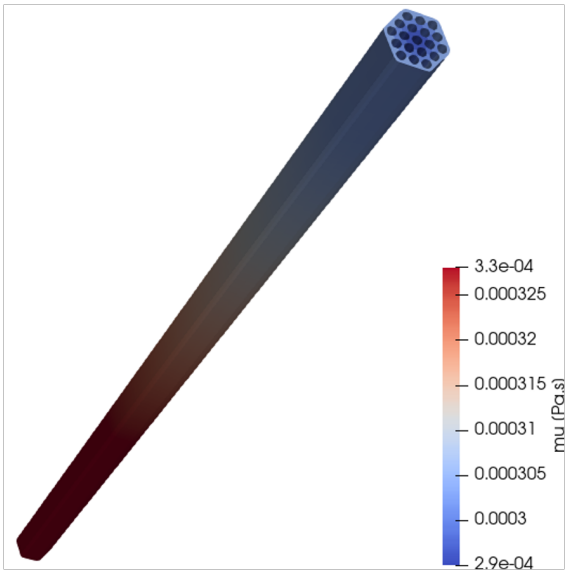

(d) Dynamic viscosity.

Figure 8: Example of simulation results for the high-flow test case in the ORNL 19-pin benchmark. (**a**) Distribution of axial mass flow. (**b**) Distribution of lateral mass flow. (**c**) Distribution of temperature. (**d**) Distribution of dynamic viscosity due to heating.

When analyzing the FFM experiments, one finds that several different combinations of power in the fuel rods and flow rates have been tried. However, in these one-phase flow cases, the temperature profile at the exit is simply regulated by the physical balance between convection

and conduction. Details on the selected cases are provided in Table 3. Therefore, it is sufficient for this brief validation exercise to only select three cases: a high flow rate, a low flow rate, and a *medium* flow rate. As the flow rate goes down, conduction dominates over convection, and the heat profiles at the exit become more uniform.

Subchannel efforts are new in Pronghorn when compared to other subchannel codes that have been developed, improved, and validated for many years. Hence, we thought it appropriate to include the results obtained by the SUBAC [35] and MATRA-LMR [36] codes in our comparison against experiments. We have selected these two codes because they have previously presented openly available results for the ORNL 19-pin benchmark and are, to our knowledge, the most developed subchannel codes for LMFRs. Including these codes allows us to have a metric of the accuracy that can be reasonably expected from a subchannel code for the ORNL 19-pin benchmark. In most works on LMFRs, the influence of the β and C_T parameters defining the turbulent mixing enthalpy and momentum cross flows, equations (51) and (53), is generally disregarded due to the large heat conduction in the liquid metal. Nonetheless, we found in our formulation that tuning these parameters allows us to fine tune the temperature distributions, yielding better results. Therefore, an optimization loop was implemented around the β and C_T parameters using the gradient descent method. The optimization metric was the average mean squared difference between the experiment measured temperature and the predicted ones of the three cases analyzed. The final optimized values encounter were $\beta = 0.121$ and $C_T = 1.236$.

We compared our results against the experimental values and SUBAC and MATRA-LMR codes in Figure 9. For every single case, our code predicts temperature distribution values that matches more closely the experimental results. Without the optimization of β and C_T, using the standard values $\beta = 0.07$ and $C_T = 1.0$, our code predictions were only slightly better than the SUBAC ones. However, after tuning the mixing coefficients, which yielded an increase in its value, our code is able to predict flatter temperature distributions that more closely matches the ones measured in the FFM experiment.

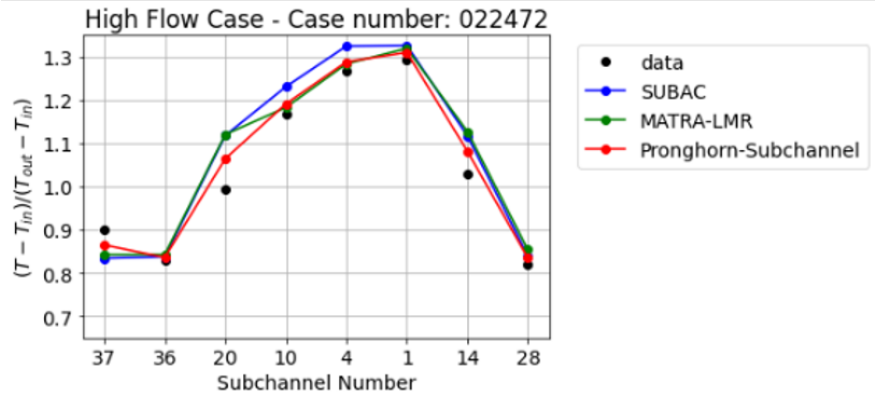

(a) High mass flow case.

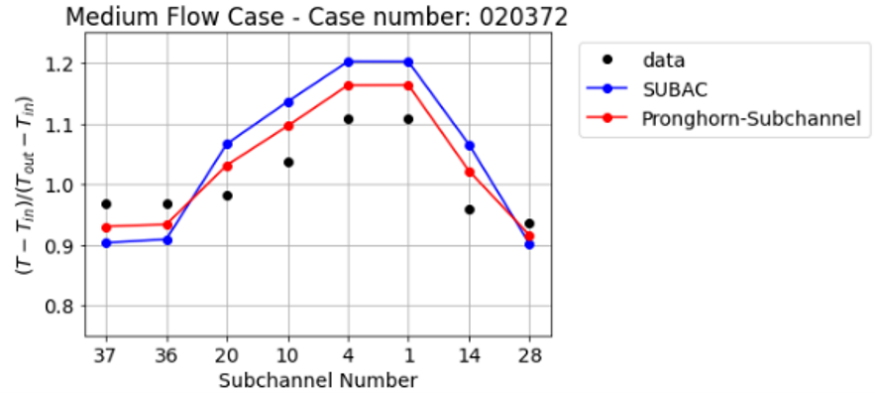

(b) Medium mass flow case.

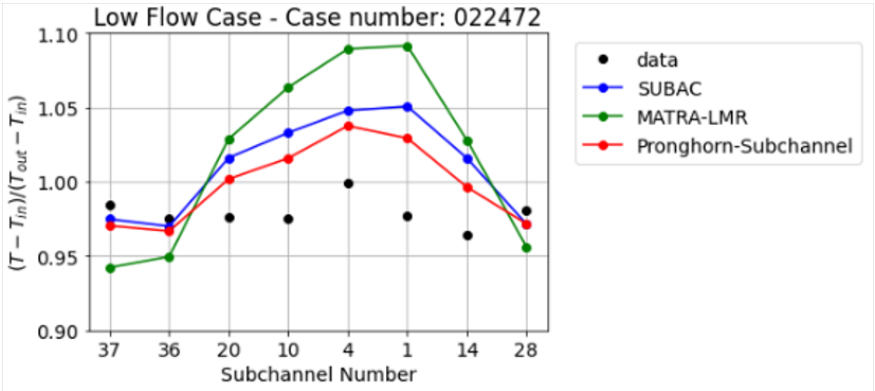

(c) Low mass flow case.

Figure 9: Comparison of results obtained for ORNL's 19-pin case between experimental measurements, the SUBAC code, the MATRA-LMR code, and the current code. (**a**) High mass flow case. (**b**) Medium mass flow case. (**c**) Low mass flow case. These results have been obtained using $\beta = 0.121$ and $C_T = 1.236$

5.2 Toshiba's 37-pin benchmark

The ORNL 19-pin benchmark allowed us to validate the code performance in a small assembly with relatively large mass flow rates. Under these conditions, radial heat conduction in the sodium is limited due to the assembly size, and in addition the thermal buoyancy has little effect on the velocity profile. To extend the validation of our models, we selected Toshiba's 37-pin benchmark [37], based on liquid-sodium experiments conducted by the Toshiba Corporation Nuclear Engineering Laboratory in Japan. It consists of a larger assembly than ORNL's 19-pin benchmark, with one more outer ring of heated rods. The specific power per rod is smaller than ORNL's 19-pin benchmark, but rods have a slightly larger diameter and a larger axial heated length, which increase the influence of thermal buoyancy in determining the flow profile.

The characteristics of Toshiba's benchmark are provided in Table 4. As for the FFM experiment, the rods are electrically heated. However, contrary to FFM, the resistances in the electrically heated rods are adapted to reproduce a chopped cosine power distribution in the axial direction. We assumed all heating rods had the same power distribution. The cross section of the fuel assembly is presented in Figure 10. This figure also describes the rod and subchannel numbering. As in the FFM experiments, the analyzed quantity of interest is the temperature distribution at the assembly outlet. Due to symmetry, it is enough to analyze the temperature distributions over a symmetry line. In this case, following reported results, we take a south-to-north line in the fuel assembly, which involves, in south-to-north ordering, Subchannels 72, 49, 32, 20, 10, 4, 3, 2, 1, 7, 14, 26, 39, and 58.

Similar to the previous 19-pin benchmark, we selected three flow configurations with a reducing axial mass flow rate for the validation exercise. Note, however, that the high-flow-rate case presents a significantly smaller flow rate than ORNL's 19-pin benchmark. Therefore, the temperature profiles for the high-flow-rate case will be flatter for the high flow case in the present benchmark.

An example flow distribution for the high-flow-rate case is depicted in Figure 11, which shows a flatter temperature profile obtained in the bulk of the fuel assembly when compared to the ORNL's 19-pin case. However, in this experiment, the ratio of gap distance to pitch is larger than the 19-pin benchmark case. This produces a significantly larger mass flow in the outer

Experiment Parameter (unit)	Value
Number of pins (-)	19
Rod pitch (cm)	0.726
Rod diameter (cm)	0.584
Wire wrap diameter (cm)	0.142
Wire wrap axial pitch (cm)	30.48
Flat-to-flat duct distance (cm)	3.41
Inlet length (cm)	40.64
Heated length (cm)	53.34
Outlet length (cm)	7.62
Outlet pressure (Pa)	1.01E5
Inlet temperature (K)	588.5
Power profile (-)	Uniform

Table 2: Design and operational parameters for ORNL's 19-pin benchmark.

Naming	Run ID	Rod Power (W/cm)	Flow Rate (m^3/s)	Reynolds Number
High flow rate	022472-hf	318.2	3.47E-03	6.72E4
Medium flow rate	020372	30.8	3.15E-04	7.35E3
Low flow rate	022472-lf	4.9	4.67E-05	9.05E2

Table 3: Validation cases selected in the ORNL benchmark.

Experiment Parameter (unit)	Value
Number of pins (-)	37
Rod pitch (cm)	0.787
Rod diameter (cm)	0.650
Wire wrap diameter (cm)	0.132
Wire wrap axial pitch (cm)	30.70
Flat-to-flat duct distance (cm)	5.04
Inlet length (cm)	—
Heated length (cm)	93.0
Outlet length (cm)	—
Outlet pressure (Pa)	1.01E5
Inlet temperature (K)	Experiment dependent
Power profile (-)	Chopped cosine (peaking factor 1.21)

Table 4: Design and operational parameters for Toshiba's 37-pin benchmark.

Naming	Run ID	Rod Power (W/cm)	Inlet Temperature (K)	Flow Rate (m^3/s)	Reynolds Number
High flow rate	B37P02	15.57	484.3	1.48E-03	1.12E4
Medium flow rate	0C37P06	11.92	476.5	3.34E-04	2.81E3
Low flow rate	E37P13	3.89	479.4	1.07E-04	7.39E2

Table 5: Validation cases selected in Toshiba's 37-pin benchmark.

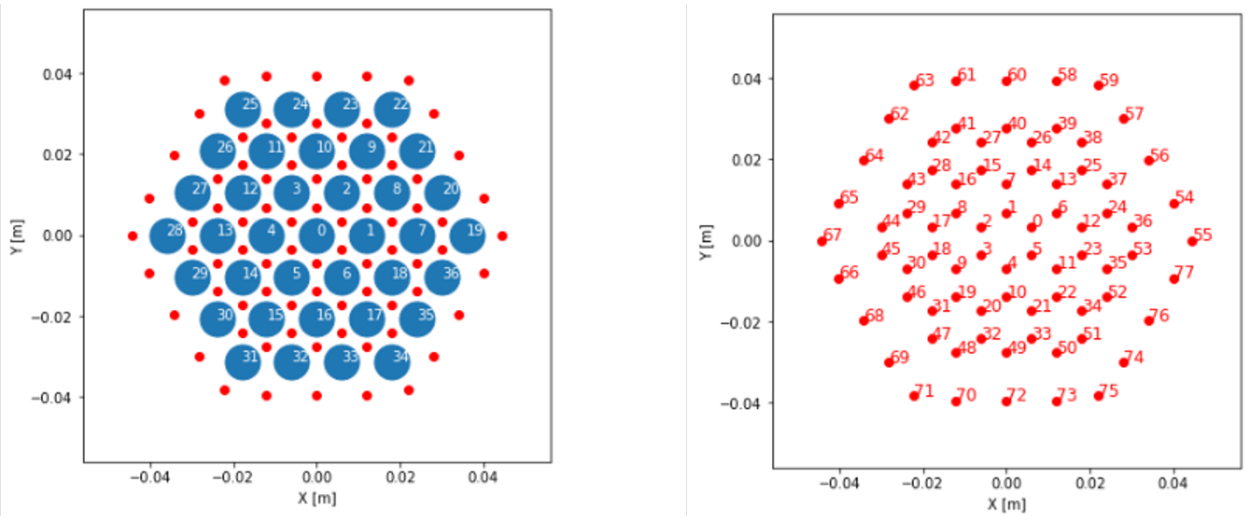

(a) Rod positions.

(b) Subchannel positions.

Figure 10: Rod and subchannel positions and numbering adopted for the Toshiba 37-pin benchmark. (**a**) Position and numbering of the heated rods with the subchannel center indicated with red dots. (**b**) Center position and numbering of the subchannels.

subchannels, as observed in Figure 11a. This causes the outer subchannnels to be significantly colder than the ones in the center. Thus, the expected temperature distribution is a flat distribution in the central region of the assembly with sharp drops next to the wrapper. Finally, it can be observed in Figures 11a and 11b that, due to the significant difference between flow rates at the outer and center subchannel, there is a considerable flow development length in the entry to the fuel assembly. Inlet velocity conditions were unclear in the experiment report [37], and hence, we assumed a uniform mass flow at the inlet. If the assumption of uniform inlet flow rates turns out to be incorrect, we expect a small deterioration in the accuracy of the predicted outlet temperature. However, we observed that the flow rates fully develop before the outlet of the assembly, which suggests that this initial condition will have little effect over the analyzed temperature distribution there.

The results obtained for the high-, medium-, and low-flow-rate validation cases are presented in Figure 11. As in ORNL's 19-pin case, we compared the results obtained with the present code with the ones obtained in the experiments and SUBAC code [35]. We have selected SUBAC for the code-to-code comparison since it is, to our knowledge, the only subchannel code for wire-wrapped SFRs, with openly available results, that presented the best agreement between the code predictions and experiment measurements for the current benchmark. Unlike the previous

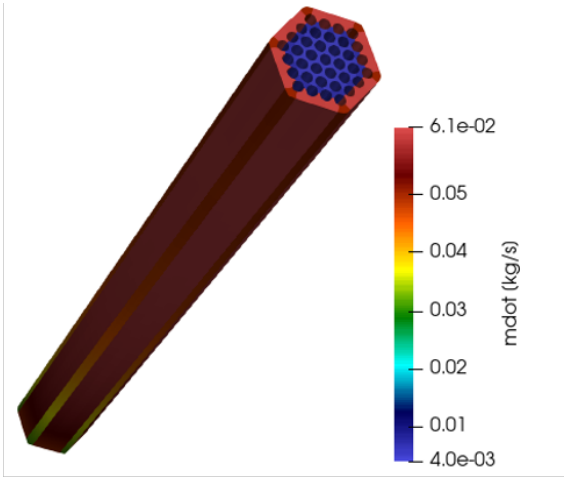

(a) Axial mass flow.

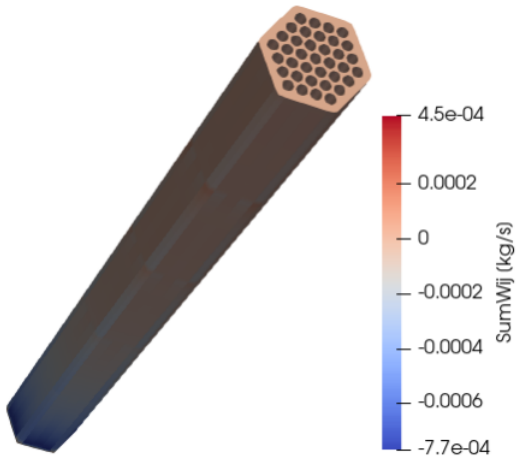

(b) Lateral mass flow.

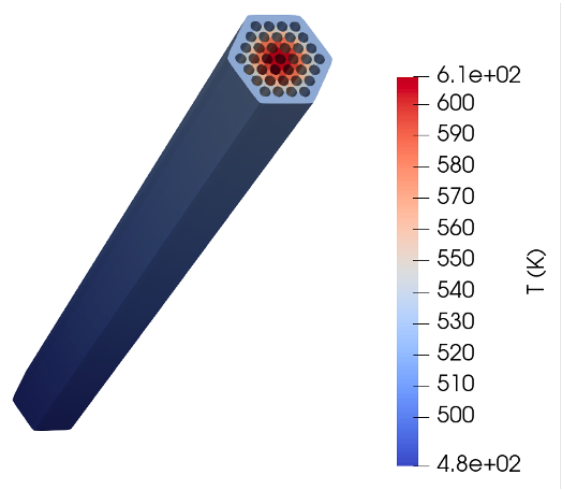

(c) Temperature.

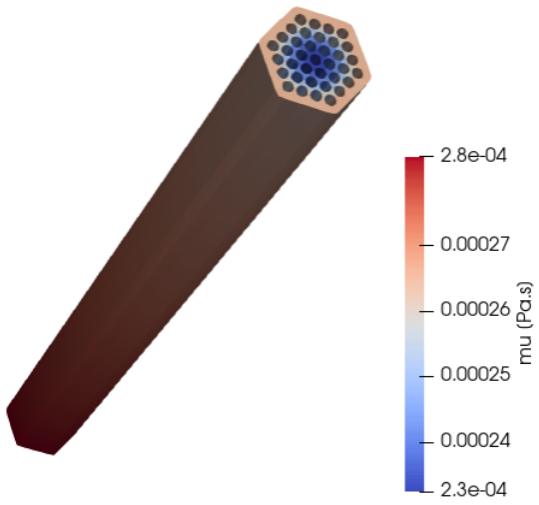

(d) Dynamic viscosity.

Figure 11: Example of simulation results for the high-flow test case in the Toshiba 37-pin benchmark. (**a**) Distribution of axial mass flow. (**b**) Distribution of lateral mass flow. (**c**) Distribution of temperature. (**d**) Distribution of dynamic viscosity due to heating. These results have been obtained using $\beta = 0.121$ and $C_T = 1.236/$

benchmark, we did not fine-tune β and C_T for the present case. We did use the same $\beta = 0.121$ and $C_T = 1.236$ as in the previous case since we want this exercise reproduce what vendors may expect in a preliminary design context on which experiments for the specific assembly may not be readily available, and hence, they must on a best estimate for β and C_T.

As observed in Figure 12, for the high-flow-rate case, the present model predicts results closer to the experimental results than SUBAC. We expected this, since the turbulent cross-flow calibration developed in ORNL's 19-pin case should still improve the prediction for the present case. However, when comparing the results predicted for the medium- and low-flow-rate cases in Figures 12b and 12c, respectively, we observed that our models overpredict the temperature distributions compared to SUBAC. Further analysis determined that the more peaked temperature distribution predicted by PrSub towards the center of the assembly may be produced by an overprediction of mixing rates, which yields larger than expected flows in the outer channels. This assessment led us to slightly decrease the values of β and C_T, resulting in flatter temperature distributions in the outlet of the assembly, which more closely matched experimental results. This leads us to suggest that best-estimate values of β and C_T can be used for scoping analyses, but a calibration of β and C_T is needed for a particular geometry when using the present code for engineering analyses purposes.

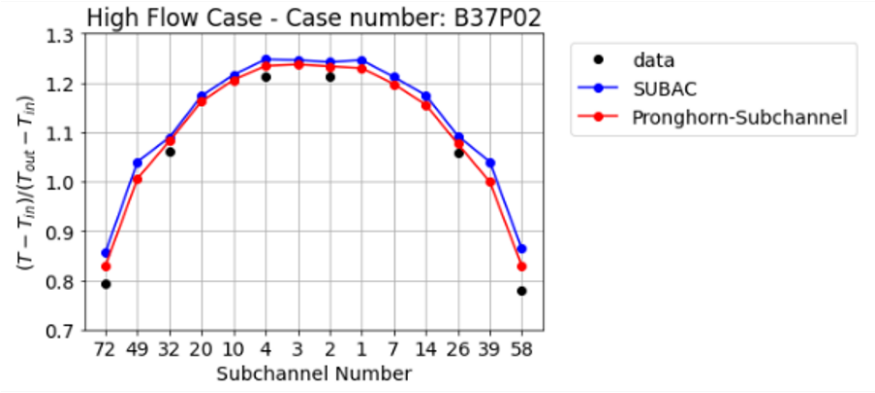

(a) High mass flow rate case.

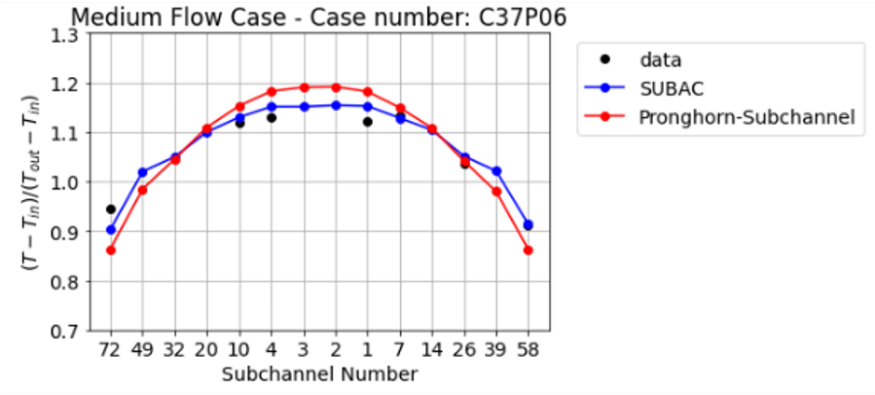

(b) Medium mass flow rate case.

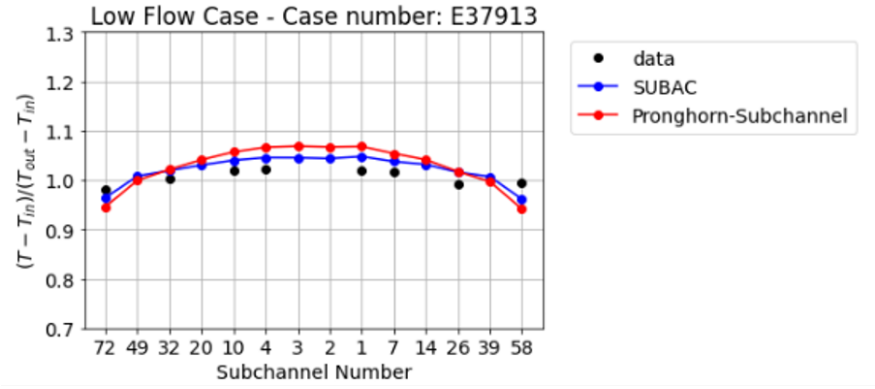

(c) Low mass flow rate case.

Figure 12: Comparison of results obtained for Toshiba 37-pin case between experimental measurements, the SUBAC code, and the current code. (**a**) High mass flow case. (**b**) Medium mass flow case. (**c**) Low mass flow case.

In summary, two benchmark cases have been analyzed in this section: the ORNL 19-pin case and Toshiba's 37-pin case. In both cases, three experiments with high, medium, and low rates have been selected to test the code with different ratios of heat convection over heat conduction in liquid sodium. We observed PrSub's accuracy and performance to be comparable to modern

subchannel codes that have been developed specifically for SFR analysis. Moreover, we have shown that calibration of the turbulent mixing coefficients can yield code predictions that better match experimental results than these subchannel codes. However, we then demonstrated that calibration of turbulent parameters must be redone for every specific geometry, as one set of parameters does not extrapolate well to different assembly designs. For engineering analyses, we suggest calibrating the turbulent mixing coefficients to the studied geometry. However, should specific experiments not be available, using best estimates for the turbulent mixing coefficients (we suggest $\beta = 0.1$ and $C_T = 1.0$) will yield results comparable to other internationally validated subchannel codes. The following sections present analyses for realistic SFR rod bundles with 217 pins. Since we have not calibrated our subchannel code for this configuration, the results presented should only be used for code capability demonstration and not for engineering design or analyses purposes.

6. Porous Flow Modeling Results

The porous flow capabilities are demonstrated for test cases based on the ABTR specifications in Reference [4]. The geometry of the fuel and control elements of the ABTR along with other overall core parameters are listed in Table 6.

Parameter	Fuel Element Value	Control Element Value
Number of pins	217	91
Clad outer diameter	8×10^{-3}	1.11×10^{-2}
Pin-to-pitch-diameter-ratio	1.13	1.124
Wire-wrap diameter	1.03×10^{-3}	0 (deviation from [4])
Assembly pitch	14.598×10^{-2}	14.598×10^{-2}
Duct thickness	0.3×10^{-2}	0.3×10^{-2}
Inter-assembly gap	0.4×10^{-2}	0.4×10^{-2}
Fueled length	2.6	2.6

Table 6: Design parameters of the ABTR adopted from [4]. Length units are meters.

The two test cases, a seven assembly cluster with an explicit inter-wrapper flow model and a coarser mesh 37 assembly cluster with an effective thermal conductivity model in lieu of an explicit inter-wrapper flow model, are described in Sect. 6.1 and 6.2.

The reason the 37 assembly geometry does not include explicit inter-wrapper flow models is that the current solution method in Pronghorn relies on using a direct solver (*LU* decomposition) for the linear system of equations arising at each Newton iteration. While this approach works for small- to medium-sized problems, its execution time increases very quickly in three-dimensional problems. Currently, a native segregated solver is being implemented in MOOSE that will alleviate this problem.

6.1 Seven Assembly Cluster with Explicit Inter-wrapper Flow Model

The seven assembly cluster model is a significantly simplified model of a portion of the ABTR core, where six fuel elements surround a control assembly with partially withdrawn control rods. The model is presented for capability demonstration only and no engineering conclusions should be drawn from it. The top-down view of the seven assembly cluster is shown in Figure 4 (left, higher fidelity approach). A cut through of the geometry normal to the x-axis is shown in Figure 13. Parameters characterizing the various regions indicated in Figure 13 are listed in

Table 7. For the seven-element model, we selected the second approach described in Reference [5] to assign porosity to rodded regions (both in the fuel and control assemblies). In this approach, the flow area within the duct is divided into an inner and outer region. The outer region is delineated by a hexagon that passes through the centers of the outermost ring of pins on the one side and the duct walls on the other side; the remaining area belongs to the inner region. Different porosities are assigned to the two regions, which are detailed separately in Table 7 in the format $(\gamma_{\text{inner}}, \gamma_{\text{outer}})$. The correlations used to describe pressure drop, convective heat transfer, and effective thermal conductivity are listed by region in Table 8. The material properties for the sodium, wrapper, and pin solid materials are listed in Table 9.

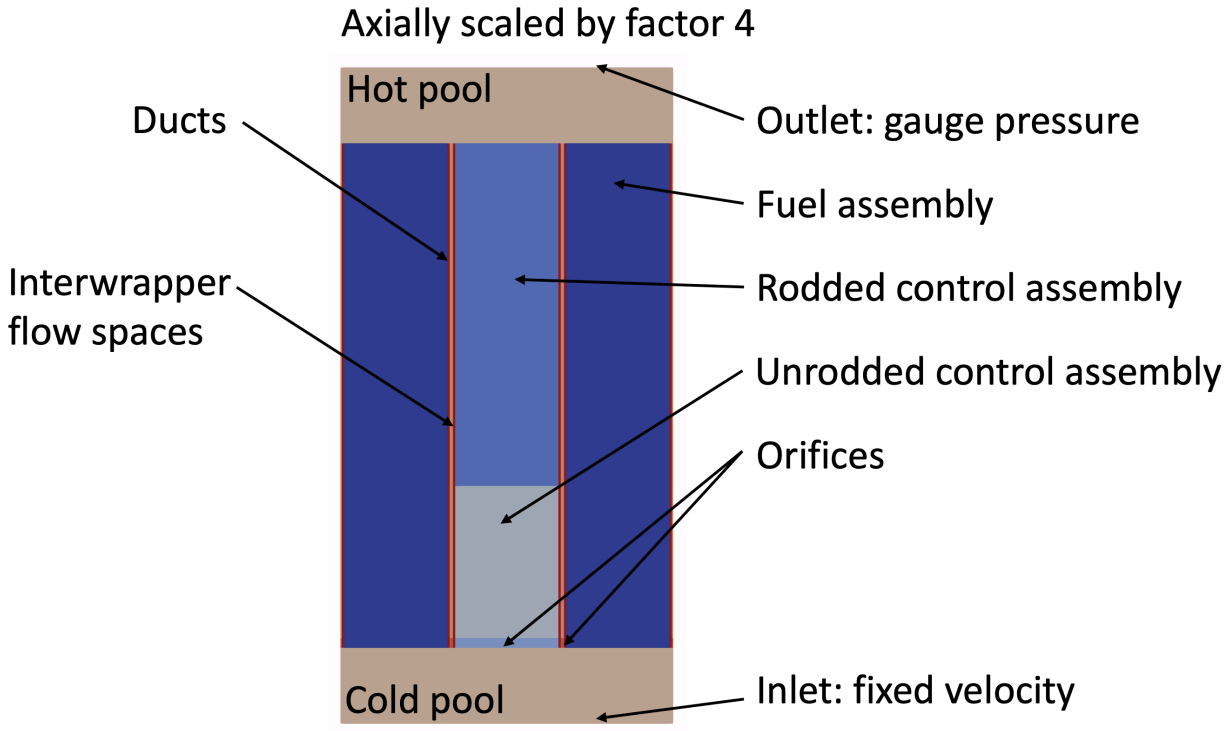

Figure 13: Cut orthogonal to the x-axis through the seven-element model. The geometry is shrunk by a factor of four in the axial direction.

A uniform heat source of 10^8 W/m^3 is applied in the fuel elements leading to a power of roughly 4.2 MW per fuel element (note, this heat source is spread over the entire volume and not just the solid fraction of the fuel elements). A total mass flow rate of 147.2 kg/s enters over the fixed velocity inlet boundary at a fixed 628.15 K. The outlet pressure is set to 0 Pa. At the given condition, the temperature rise over the core is expected to be 135 K, which is slightly smaller than

Region	D_h [m]	γ	Temperatures
Cold pool	0.34	1	F
Hot pool	0.34	1	F
Fuel assembly	0.003	(0.278,0.47)	FS
Rodded control assembly	0.008	(0.282,0.74)	FS
Unrodded control assembly	0.146	1	F
Control assembly orifice	0.146	0.5	F
Inter-wrapper orifice	0.008	0.5	F
Inter-wrapper flow space	0.008	1	F
Ducts	—	—	S

Table 7: Parameters for each region of the porous flow seven-element model. The rodded portions of both the fuel and control assemblies are split into two porosity regions following the approach from Reference [5]. The *Temperatures* column indicates if it defines fluid (F), solid (S), or both (FS) temperatures.

Region	Drag	Heat Transfer	Effective Thermal Conductivity
Cold pool	Churchill	—	Equation 76
Hot pool	Churchill	—	Equation 76
Fuel assembly	Rehme	Equation 79	Equations 77 and 78
Rodded control assembly	Rehme	Equation 79	Equations 77 and 78
Unrodded control assembly	Churchill	-	Equation 76
Control assembly orifice	Equation 84	—	Equation 76
Inter-wrapper orifice	Equation 84	—	Equation 76
Inter-wrapper flow space	Churchill	-	Equation 76
Ducts	—	Lyon-Martinelli (across boundaries to fluid)	—

Table 8: Correlations used for drag, heat transfer, and effective fluid thermal conductivity in the various regions.

Material	Thermal Conductivity W/m-K	Viscosity Pa-s	Specific Heat Capacity J/kg-K	Density kg/m^3
Sodium	65 (isotropic)	2.27×10^{-4}	1,260	820
Wrapper (steel)	20 (isotropic)	-	300	7,800
Rods	10 along rods 0 in x-y plane	-	300	15,000

Table 9: Material properties of sodium, wrapper, and "rod" materials. Note, that the different rods (fuel and control) were not distinguished but would have different material properties in a more realistic model. The constant material properties are no limitation of MOOSE and are just selected for convenience.

the 155 K for ABTR.

We present the superficial velocity in the z-direction, the pressure, and the duct temperatures at steady state for two different values of orifice coefficients $C = 300$ (large inter-wrapper and control element flow) and $C = 500$ (nominal inter-wrapper and control element flow) in Figures 14– 16.

The loss coefficient at the inlet of the control element and inter-wrapper space allows researchers to model engineered orifices. The superficial velocity in the control assembly drops from about 0.7 m/s to 0.2 m/s when increasing the loss coefficient from 300 to 500. Almost the entire pressure drop between the hot and cold pool in the inter-wrapper flow spaces occurs over the orifice regions. The pressure drop of 180 kPa appears reasonable for the geometry and flow rates, but additional testing should be performed to confirm that all pressure drop correlations are implemented correctly.

The strong discontinuity in body forces in the orifice region leads to some oscillations in the velocity field despite using Pronghorn's approach to suppress oscillations described in Reference [22]. Without these methods, the oscillation would be much more severe. Future work will investigate if grid refinement in combination with changes in the parameters controlling the oscillation suppression algorithms removes the oscillations. In addition, we will investigate if these oscillations pose problems to the accuracy of the solution. It is noted that, to the author's knowledge, all commercially available or open-source collocated FVM codes suffer from oscillations at sufficiently strong body force and porosity interfaces.

The ducts around the fuel elements are significantly hotter than the duct around the control element. In addition, the sides of the fuel element duct facing the control element are cooler than the sides that face away from the control element. The different flow rates for the $C = 300$ and $C = 500$ cases in the control element and the inter-wrapper space have a small but measurable effect on the wrapper temperatures (7 K at the outlet). Figure 16 shows that Pronghorn is capable of modeling the distribution of duct temperatures in the core given orifice coefficients and a power distribution. Coupling with MOOSE's tensor mechanics module allows researchers to deduce deformation from the computed duct temperatures.

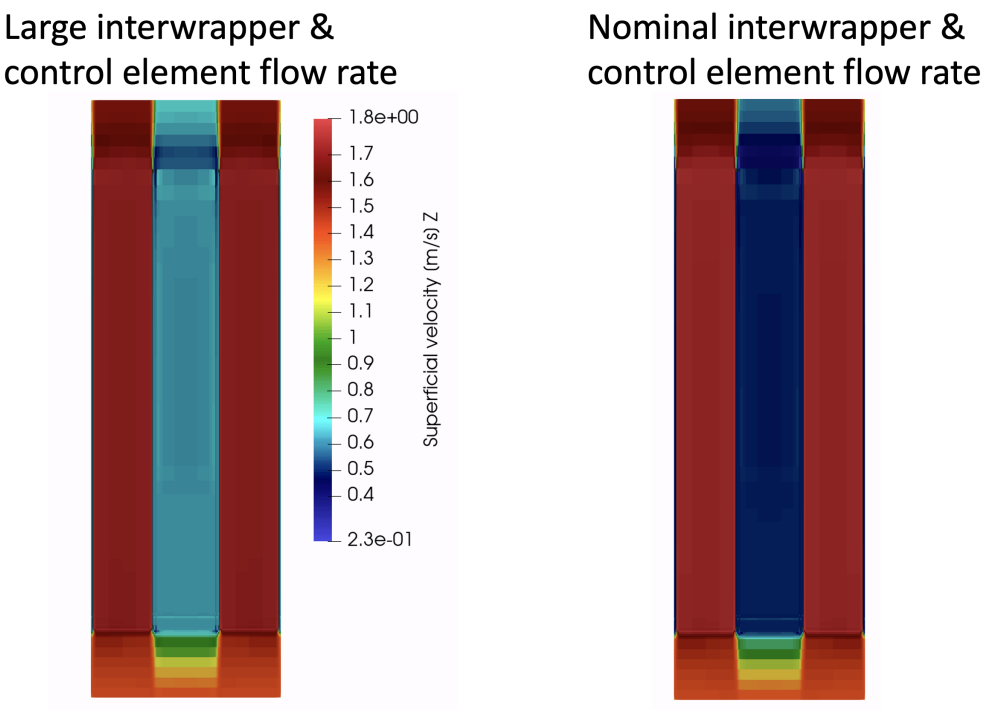

Figure 14: Superficial velocity in the z-direction for large ($C = 300$) and nominal bypass flow ($C = 500$).

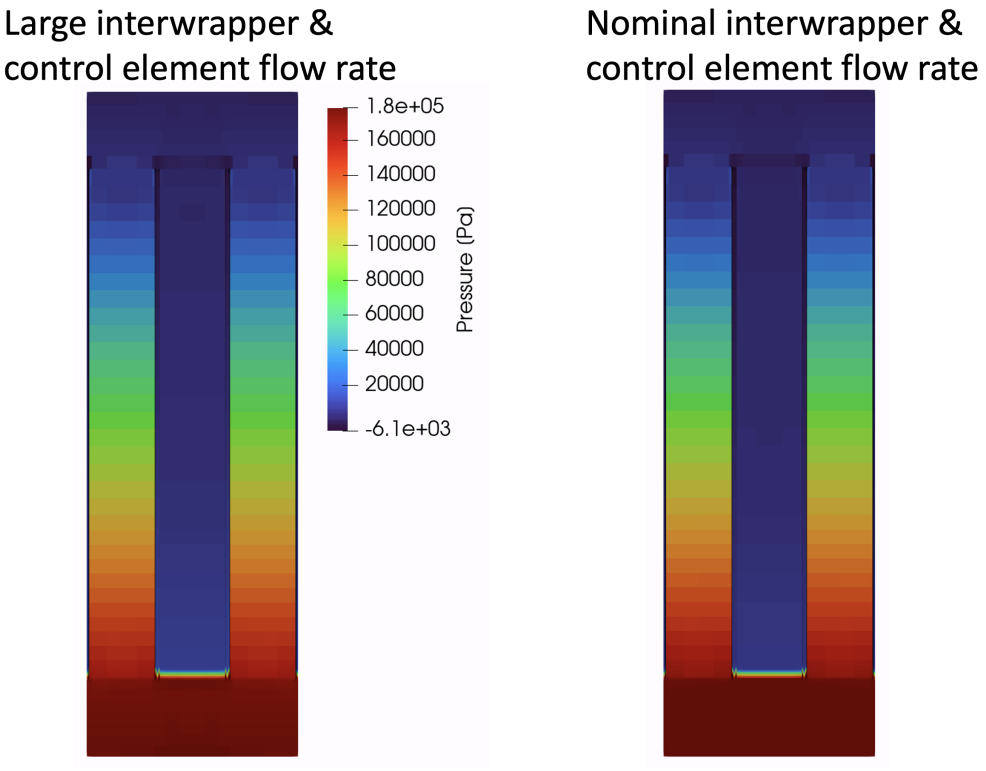

Figure 15: Pressure distribution for large ($C = 300$) and nominal bypass flow ($C = 500$).

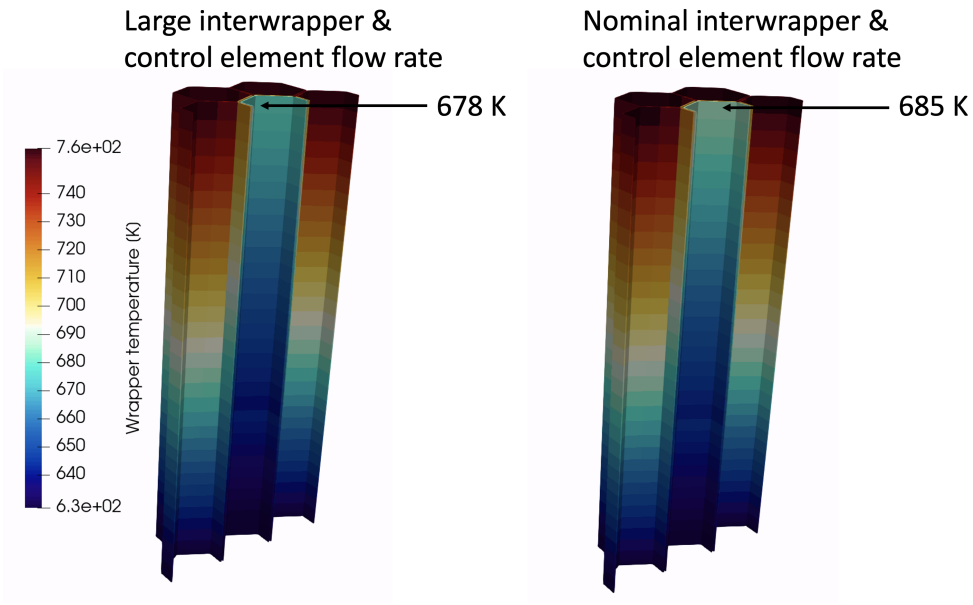

Figure 16: Duct temperature distribution for large ($C = 300$) and nominal bypass flow ($C = 500$).

6.2 37 Assembly Model

In contrast to the seven-element model, the 37 assembly model does not explicitly model the inter-wrapper flow, and it uses a single porosity region for the rodded portion of the fuel and control elements. The geometry of the 37 assembly model is depicted in Figure 17. The flow enters downwards through the inlet boundary and leaves the domain upward through the outlet boundary.

The parameters, correlations, and material properties used for the seven-element case are still used except:

- The porosity in the fuel element is 0.31 and 0.45 in the rodded control element.
- The inter-wrapper region is filled with a fictitious material with the following thermal properties: thermal conductivity $k = 40$ W/m-K, specific heat capacity $c_p = 300$ J/kg-K, and density of $\rho = 2,000$ kg/m^3; these material properties likely do not represent the heat transfer through the duct and the inter-wrapper space well. No flow is allowed in the inter-wrapper flow region and the wrappers exchange heat with the inter-wrapper region via conduction.
- An additional region for modeling the control rod tip is present, where the pressure drop is

computed using Equation 87 with $\gamma_o = 0.45$ and $\gamma_i = 1$.

- All assemblies have orifices at their inlets and Eq. 84 is used in these regions, but with possibly different values of C.

A uniform downward velocity is applied at the inlet boundary leading to a mass flow rate of 831.6 kg/s, a gauge pressure boundary condition is applied at the outlet. All fuel assemblies have the same power density, while control assembly have no power density applied to them.

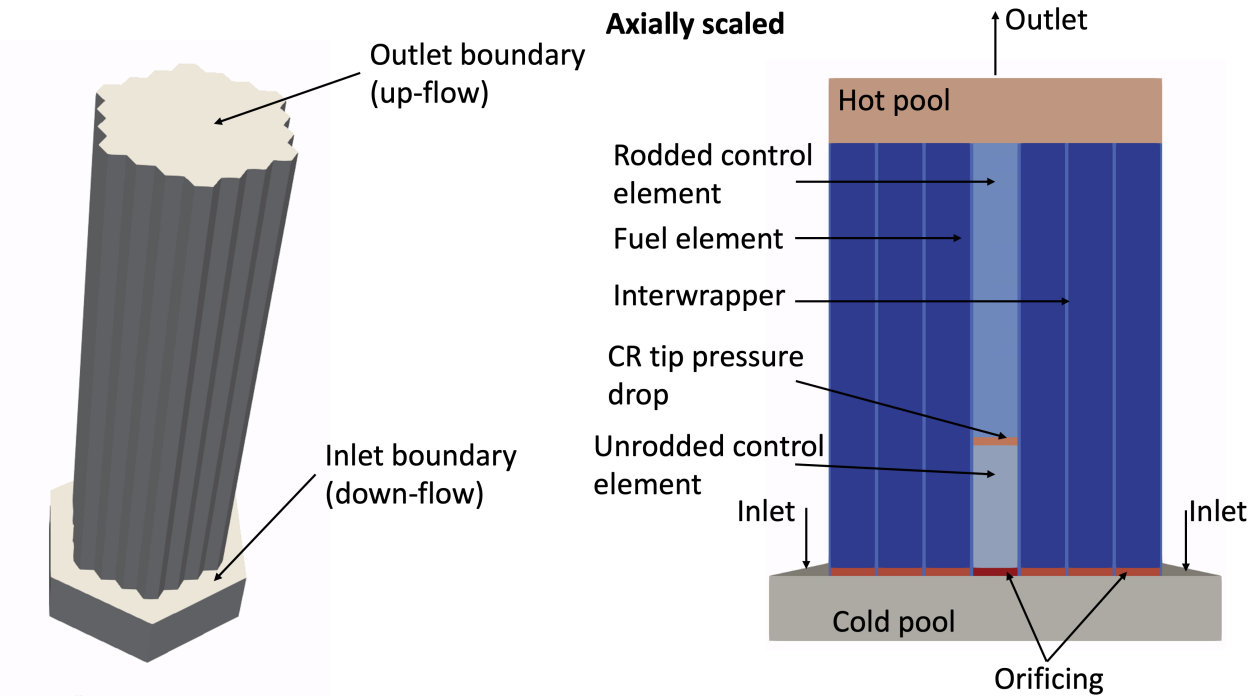

Figure 17: Cut orthogonal to the x-axis through the 37 assembly model.

The steady-state distribution of superficial velocity in the z-direction and temperature (fluid temperature wherever it is defined and "solid/mixture" temperature in the duct/inter-wrapper space) are shown in Figure 18. The fluid enters the cold pool as downflow with a negative velocity, then turns in the cold pool and enters the assemblies. The control assemblies have orifices with large pressure drop coefficients at the inlet, resulting in a superficial velocity less than half of the flow rate in the fuel assemblies. Pronghorn performs well in suppressing unwanted oscillations at the interface between the cold pool (almost no drag and free flow) and fuel assemblies (Rehme drag and much smaller porosity) and between the rodded and unrodded parts of the control rod element using the methods described in Reference [22]. Residual oscillations remain at

the orificing region before the control assemblies. These result from very large Forchheimer coefficients (about 4,000) right next to essentially free-flow conditions (Forchheimer is zero). Currently, these oscillations are under investigation to determine if very coarse meshes, in conjunction with the oscillation suppression method in Reference [22], can in principle remove the oscillations. In general, the problem can be solved by additional mesh refinement around a very strong pressure drop region, but this avenue will not be available for Pronghorn's porous flow model until native MOOSE segregated solvers have been fully deployed.

From the temperature distribution, it is obvious that (as expected) the control assemblies are significantly colder than the fuel assemblies. However, heat is transferred from the fuel assemblies to the control assemblies via conjugate heat transfer and conduction through the duct/inter-wrapper space, which can be seen by comparing the inlet and outlet temperatures of the control assemblies. The fuel elements to the outside of the 37 assembly cluster have a slightly hotter outlet temperature than the channels in the interior because very few of the fuel elements are neighbors to cool control elements; this is to a small degree compounded by slightly higher flow rates through the central flow assemblies due to the way the flow turns in the cold pool.

The total pressure drop over the core is 420 kPa, which seems high but might be related to the comparatively large mass flow rate through the system. Among other things, the large mass flow rate leads to an average temperature rise of the fluid in the presented model of only about 125 K, when in ABTR it is about 30 K more.

The results in this section demonstrate that Pronghorn can model multi-fuel-element SFR geometries using porous flow with and without explicit inter-wrapper flow spaces. The resolution obtained with porous flow models is naturally lower than what is obtained with subchannel codes so the goal of porous flow modeling is to model large portions of the core or the entire core. The porous flow method can capture core-wide gradients of flow distribution, fluid temperatures, and duct temperatures. The results in this section demonstrate that Pronghorn has the capabilities required to perform this task. However, performance bottle necks need to be removed and the method must be tested and pass VBV to lift it to full production level status.

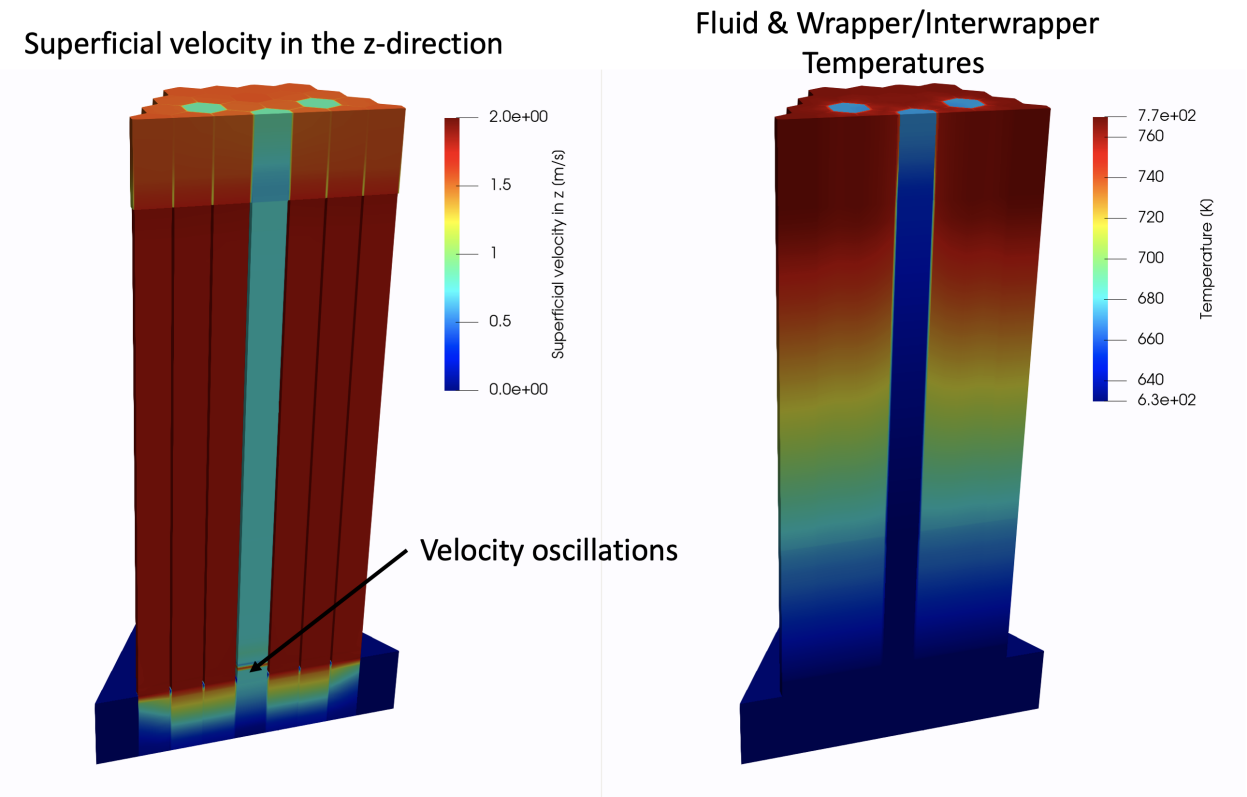

Figure 18: Superficial velocity in the z-direction (left) and temperature (right) at steady state for the 37 assembly problem solved with porous flow. The temperature is the fluid temperature everywhere except in the wrapper/inter-wrapper region where it is the ”solid” temperature.

7. Coupling PrSub, Bison, and Pronghorn

A key part of the interest of integrating a subchannel code into Pronghorn is the ability of MOOSE to couple with different physics. For LMFR modeling, the key value added proposition is to couple PrSub with Bison for fuel performance and with Pronghorn for mixed subchannel and 3D-porous flow simulations (e.g., the inter-wrapper flow is modeled using Pronghorn, while the assemblies are solved using PrSub). This section is organized as follows. First, we demonstrate the conjugate heat transfer between a Bison fuel pin and duct heat conduction model with the subchannel intra-element flow solution using the 37-pin Toshiba benchmark as example. Then, a fuel assembly inspired by the ABTR containing explicit modeling for the fuel pins, subchannels, and duct is thermally coupled to the 37-element porous model. We study the following three cases:

- A low-flow and a high-flow steady-state configuration
- A transient case where a power burst is introduced into a single pin.

Finally, we close this section by demonstrating an online coupling of PrSub with Pronghorn's porous flow model. Note that our results here are not meant to be realistic but rather to showcase the functionality of the code.

7.1 Demonstration of the Thermal Coupling Methodology in One Fuel Assembly

PrSub computes the thermal-hydraulics fields defined on the fluid domain located between the pins and the ducts. However, heat conduction in the fuel pins and duct may cause differences in the heat fluxes entering the fluid domain and, hence, affect the subchannel solution. To increase fidelity in modeling LMFRs, part of the effort in this milestone has been devoted to coupling PrSub to Bison and the heat conduction module in MOOSE. The coupling has been performed using MOOSE's MultiApp system. The available set of MOOSE's multi-app transfers has been used, except for a new transfer that has been developed to map 2D-*rz* cylindrical simulations of the fuel pins to the 3D subchannel solution.

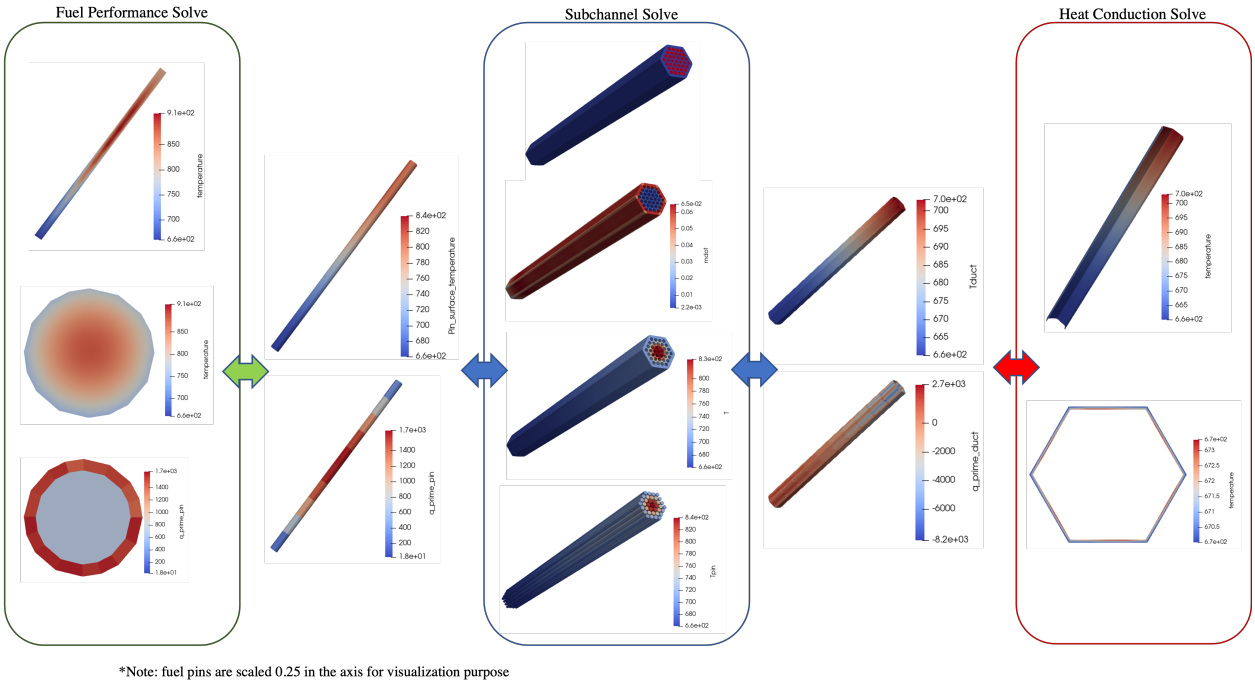

Figure 19: Demonstration of an assembly coupling methodology between fuel performance, subchannel, and heat conduction for the 37-pin benchmark.

An example of the coupling methodology for Toshiba's 37-pin benchmark (Figure 10) is presented in Figure 19. The subchannel solve is the main application of this multi-application system. Assuming a linear heat profile for each of the fuel pins and the duct, a subchannel solve is performed. A full solution to the tolerance limit is developed for steady-state coupling, while a converged time step solve is performed for transient coupling. The subchannel solution computes the axial and lateral mass fluxes, pressure profile, and enthalpy. Using the latter two, temperature within each subchannel is computed. Next, the subchannels next to the fuel rods and duct are parsed and the temperature at the rods and duct surface, respectively, are computed using the heat transfer correlation. These surface temperatures are transmitted to the pins and duct applications as shown in Figure 19. For each fuel pin, a separate Bison calculation is performed, which involves a heat conduction problem with an internal heat source. A uniform thermal conductivity is used in the fuel pins for this demonstration problem. However, in the actual problem, the fuel pins will have a smaller conductivity in the axial direction due to the contact between fuel pellets. This calculation has been done in 3D in this work but 2D-*rz* models can be used when symmetry is assumed in the subchannel flow field and, hence, in the surface

temperature. As a result of the Bison calculation, a new linear heat generation rate profile is obtained at the surface of each pin. This profile is returned to the subchannel application, which now repeats its solve step with updated linear heating rates. The coupling at the duct surface is performed in a similar manner as for the fuel pins, except that the coupling also involves a significant azimuthal component as temperatures over the cross section of the duct can vary significantly. For this purpose, a separate grid has been constructed at the duct-subchannel surface, which allows the MultiApp system to map the linear heat generation rates into a position that can be directly transferred to the outer subchannels. This duct mesh is shown in Figure 20 along with the pins and subchannels in the assembly. Once the linear heat rates are computed in the center points of the duct mesh, they can be directly transferred to the adjacent subchannels as there is a 1-to-1 relation between the duct and subchannel nodes.

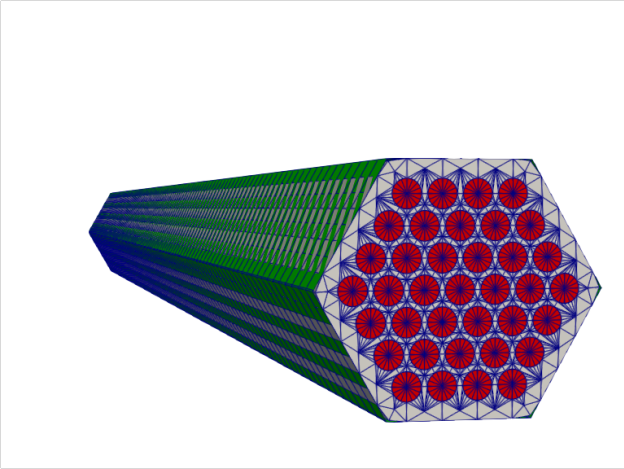

Figure 20: Example of mesh showing the fuel pins, subchannels, and the duct. Note how the duct mesh is constructed to perform a direct transfer to each of the adjacent subchannels.

7.2 High-Flow, Steady-State Analysis of One Fuel Assembly in the 217-Pin Model

The simulated fuel element for this model has been taken from the ABTR preconceptual design report [4]. Details about the fuel element and the fuel assembly are presented in Figure 21. The active part of the assembly is simulated with the coupled subchannel code, which consists of the shield, fuel, and gas plenum parts. A cross-section view of the fuel assembly is presented in Figure 22. The simulation integrates 217 identical fuel pins simulated with Bison, the subchannel

flow domain, and the external solid duct. The subchannel flow, fuel pins, and wrapper are thermally coupled. Picard iterations are performed between the temperatures and heat fluxes at these component interfaces to find the steady-state solutions. When coupling with the 37-element porous flow model, we observed that the subchannel solution had little impact on the temperatures predicted by the porous flow. Therefore, the coupling with the porous flow model for the reactor core is done with an *offline* method. In this sense, the porous-flow-computed temperature in the outer surface of the wrapper is applied as a Dirichlet boundary condition in the coupled duct-subchannel-pin model.

As can be easily seen in Figure 22, the gap-to-pitch for this fuel assembly is smaller than the ones in the ORNL's 19-pin and Toshiba's 37-pin cases. Details about the fuel assembly characteristics are provided in Table 10. The thermal-hydraulic conditions are selected to match those of the 37-element case utilized in Section 6.2. Also, the sodium coolant, rods, and wrapper (also named duct) thermophysical properties are set to those presented in Table 9. A key difference with the porous model is that two mixing grids are included in the model: one at the entry of the fuel assembly and one before the fuel section following the standard SFR design. Besides this difference, the fuel element model is identical to the one used in Section 6.2. Steady-state simulations of subchannel, duct, and fuel pins are performed and Picard iterations are carried out until convergence.

The results obtained for the thermal-hydraulics fields are depicted in Figure 23 for an axial cut joining the east-to-west vertices of the fuel assembly and in Figure 24 for a radial cut at the mid-height of the assembly. We can observe that the mass flow rate rapidly develops after the first mixing grid and, then, are virtually constant in the rest of the assembly. There is little effect of the second mixing grid in redistribution of the flow profile. However, small cross flows after the heated section are observed caused by the viscosity variation due to temperature changes. Pressure is larger towards the center of the assembly indicating that cross flows are present from the center to the outer part of the assembly. Also, pressure is larger for the corner channels, as pressure drop in these channels is slightly larger than for the edge ones. The temperature in the center of the assembly is higher than in the outer channels. This causes the pressure drop to reduce towards the center of the assembly. As a result, flow is dragged from the outer part of the assembly to the center while traversing the heated section.

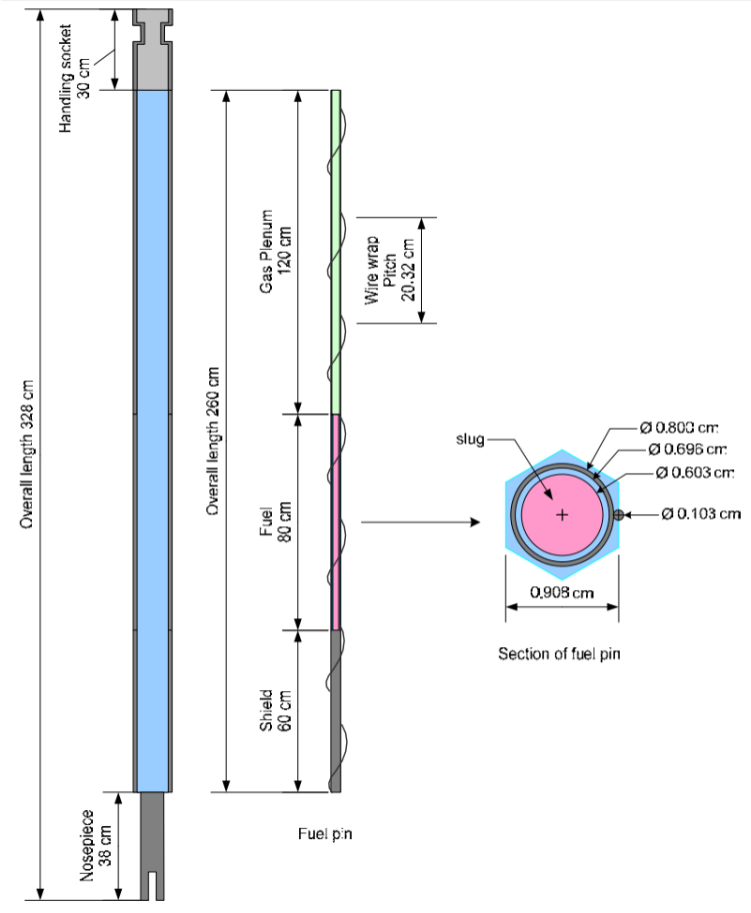

Figure 21: Details of the ABTR fuel element [4].

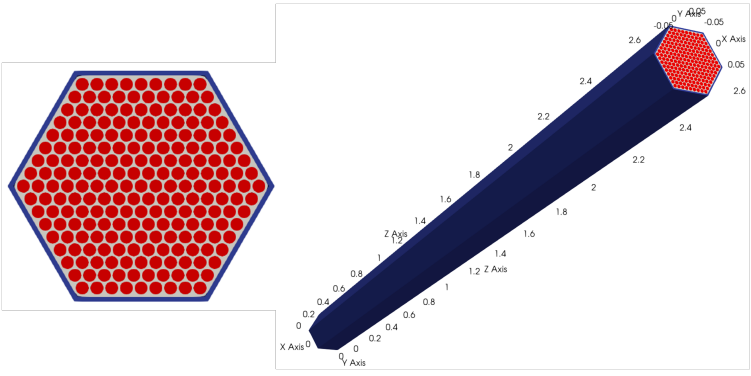

Figure 22: Left: Cross section of the simulated ABTR fuel assembly; right: 3D view of the simulation domain for the fuel assembly where the simulation domain for one assembly integrates the duct, subchannels, and fuel pin domains.

Experiment Parameter (unit)	Value
Number of pins (-)	217
Rod pitch (cm)	0.681
Rod diameter (cm)	0.603
Wire wrap diameter (cm)	0.103
Wire wrap axial pitch (cm)	20.23
Flat-to-flat duct distance (cm)	14.198
Inlet length (cm)	60.0
Heated length (cm)	80.0
Outlet length (cm)	20.32
Outlet pressure (Pa)	7.58e5
Outlet gauge pressure (Pa)	0.0
Inlet temperature (K)	628.15
Axial power profile (-)	Chopped cosine (peaking factor 1.21)
Radial power profile (-)	All fuel rods heated equally
Linear pin power (W/cm)	241.9
Inlet flow rate (m^3/s)	2.388e-2
Mixing grid positions (cm)	(20, 80)

Table 10: Design and operational parameters for the conceptual ABTR fuel assembly.

The pressure profile, as observed in Figure 23, is approximately linear in the axial direction with very small pressure drop increases at the mixing grid locations. The total pressure drop is 433 kPa, which is slightly larger that the one obtained in Section 6.2. This difference may be explained by the slight increase in the pressure drop at the mixing grids. However, this difference of about $\sim$ 3% which is within the expected uncertainty bounds of the pressure drop correlation used in the porous model. Hence, we conclude that the subchannel and porous model are able to predict similar pressure drops within the model's uncertainty. The pressure profile is approximately flat in the radial direction at the mid-height, which explains the small cross flows obtained in this direction.

Finally, Figure 23 shows that temperature mainly increases at the heated section of the fuel assembly and presents only small heating above and below this section due to heat conduction. This is mainly because of the large flow rates used in this model, which causes heat convection to be significantly larger than heat conduction. The total temperature increase in the axial direction is $\sim$ 124 K, which agrees well with the results obtained by the porous flow model in Section 6.2. This serves as a further verification of the correct preservation of the enthalpy balance in both models. The temperature profile in the radial direction is significantly larger at the center of the assembly

thanks to the larger mass flow rates obtained in the outer channels.

In summary, the mass flow rates, temperature, and pressure profiles obtained in the simulation are considered to be physical. Moreover, we find a good agreement between these profiles and the profiles obtained from the porous model in Section 6.2.

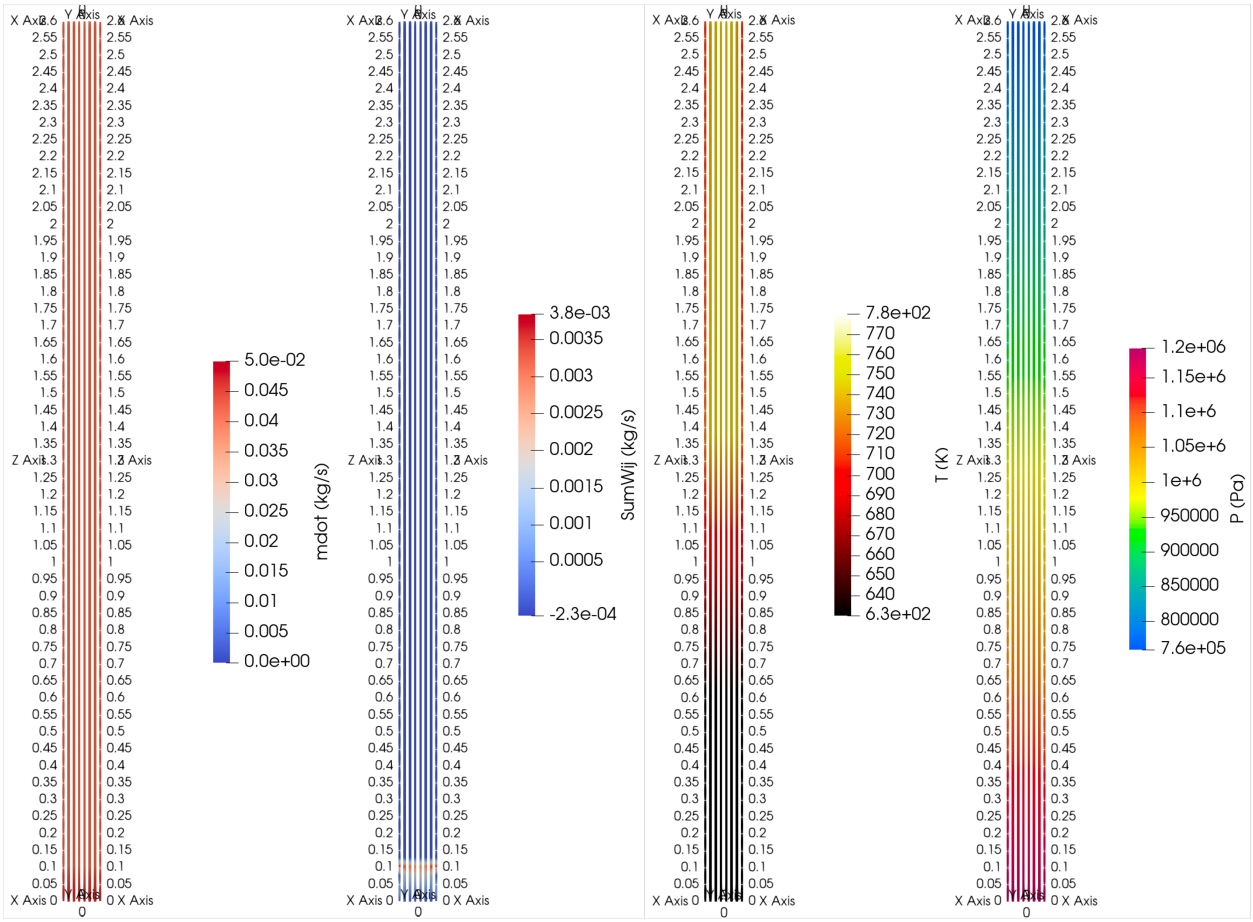

Figure 23: Axial cut of the thermal-hydraulics fields obtained for the high-flow study; left: axial mass flow rate; center-left: sum of lateral mass flow rate per subchannel; center-right: temperature; right: pressure.

The duct and central fuel pin in the assembly are analyzed next. The duct temperature profile over the outer and inner surfaces is presented in Figure 25, which shows that the predicted outer temperature is higher than the interior temperature. This is mainly a consequence of two effects. First, the subchannel model predicts slightly lower temperatures than the porous one. Second, it is an artifact of the 37-elements model, which does not explicitly resolve the inter-wrapper region and, hence, has no heat flux resistance in the inter-wrapper flow side. On the contrary, on the inner side, we model the flow resistance between the interior subchannel flow and the

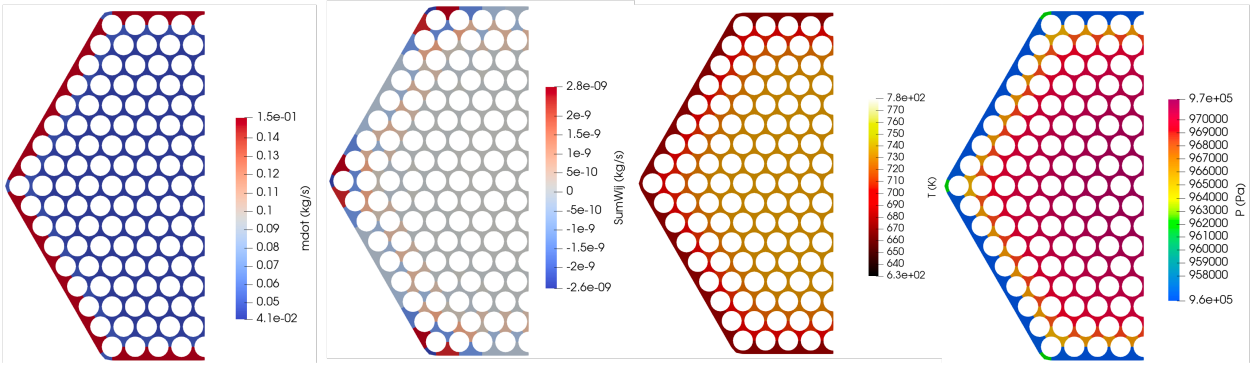

Figure 24: Radial cut of the thermal-hydraulics fields obtained for the high-flow study at $z = 1.3$m; left: axial mass flow rate; center-left: sum of lateral mass flow rate per subchannel; center-right: temperature; right: pressure.

wrapper. This leads to a predicted temperature in the interior of the wrapper that is smaller than the one predicted on the outside surface. This results will be improved in the future by refining the 37-element model to include the inter-wrapper flow and adapting the pressure drop and heat exchange correlations. However, at this point, they serve as a verification exercise in that our code is respecting the expected physics. Figure 25 also presents the linear heat fluxes coming into the fuel assembly. As expected, all heat fluxes are positive since heat is entering the assembly. Larger heat fluxes are obtained at the top part of the wrapper since the predicted temperature difference between the porous and subchannel models is larger.

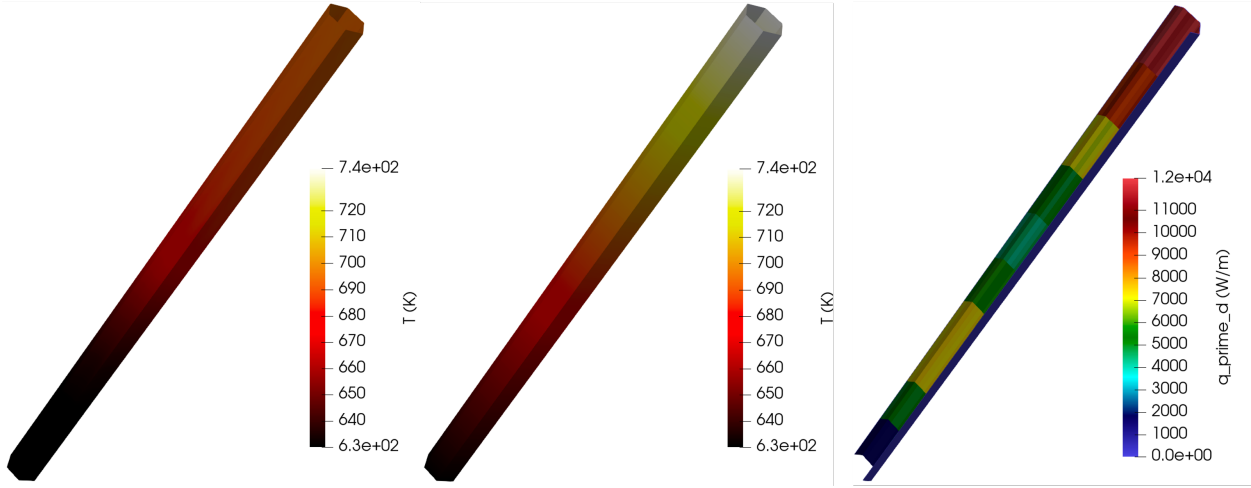

Figure 25: 3D view of the solution at the duct; left: temperature at the inner (duct-subchannel) surface; center: temperature at the outer (duct-inter-wrapper) surface; right: linear heat flux at the inner surface.

Finally, the surface temperature and linear heating rate generated for the center pin are

depicted in Figure 26. Both distributions follow the chopped cosine heat generation rate imposed in the heated region of the pin. However, some diffusive effects due to heat conduction are observed in the fuel pin, which axially homogenize temperature. In this simple model, the fuel rods have been modeled as uniform bodies of homogeneous conductivity, which should increase the effects of axial heat conduction with respect to the actual case in which conduction contact resistance between the fuel pellets is present. The surface temperature in the fuel pins is slightly larger than the subchannel flow temperature due to the flow resistance between the pin and surrounding subchannels. Finally, as expected, all heat fluxes are positive due to the heat flux leaving the fuel pins and entering the subchannel domain.

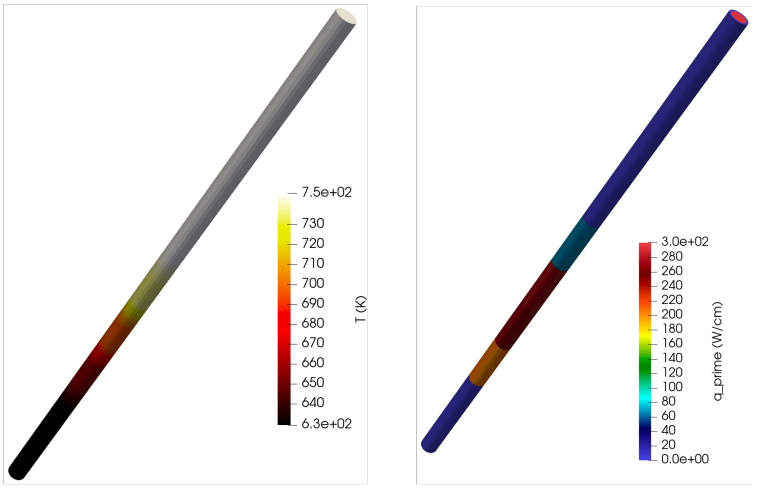

Figure 26: 3D view of the solution at the central fuel pin; left: temperature at the pin surface; right: linear heat flux at the pin surface.

In summary, this flow test has verified that the physical phenomena expected for the fuel assembly are correctly reproduced by our subchannel code. Moreover, the good agreement for the temperature rise and pressure drop between the subchannel and porous models under similar thermal-hydraulics conditions serves as extra verification for both codes. A low-flow fuel assembly is analyzed in the following section.

7.3 Low-Flow, Steady-State Analysis of One Fuel Assembly in the 217-Pin Model

In the next case, we show the capability of the subchannel code to model flow recirculation in low flow assemblies in SFRs. For this purpose, a flow condition is generated in which the internal

two rings of fuel pins in the assembly are heated and the rest of the fuel pins are assumed to generate zero power (i.e., only the internal seven rods out of the total 217 are heated). The heating profile is depicted for the fuel cross section in Figure 27, where heated rods are marked with red dots, unheated rods with blue dots, and the subchannel center position with green dots. Trying to maintain the temperature rise in the assembly and, hence, minimize the effects of the duct heat conduction to achieve flow recirculation, the total mass flow rate in the assembly is reduced to $\sim$ 3% of its value in the high flow case. The details of the fuel assembly simulation for this low-flow case are provided in Table 11.

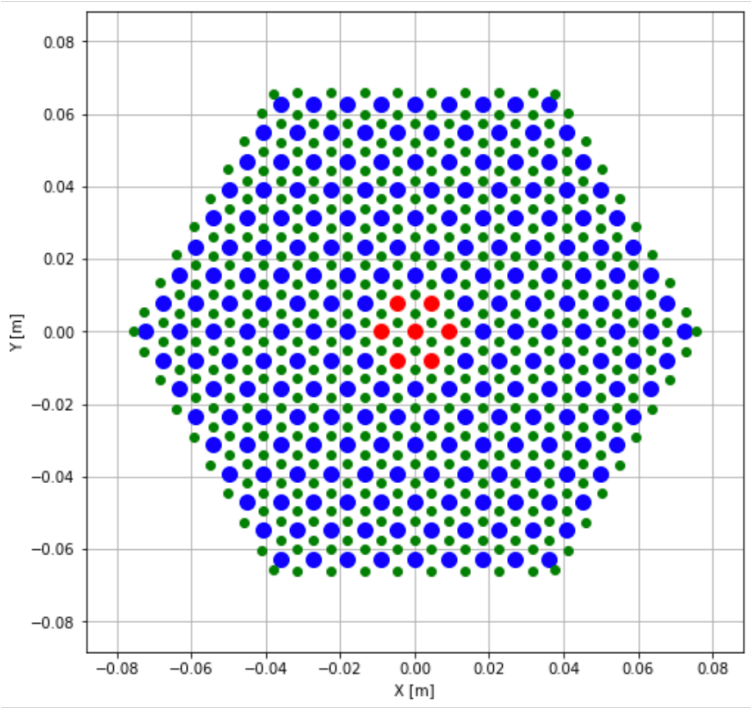

Figure 27: Cross section for the heating profile in the low-flow assembly case; heated rods are marked with red dots, unheated rods with blue dots, and the subchannels center positions with green dots.

The thermal-hydraulics solution obtained at steady-state are presented for an axial and mid-height radial slice in Figure 28 and Figure 29, respectively. Analyzing the axial cut, we can observe how a recirculation is formed in the center of the domain. Axial mass flow increases next to the heated pins, rises, and then inverts on top of the heated region. As flow rises from the center of the domain, it gets sucked into the center of the assembly by thermal buoyancy pressure. The effective cross flow is positive at the center of the subchannel as flow gets driven into the center of

Experiment Parameter (unit)	Value
Number of pins (-)	217
Rod pitch (cm)	0.681
Rod diameter (cm)	0.603
Wire wrap diameter (cm)	0.103
Wire wrap axial pitch (cm)	20.23
Flat-to-flat duct distance (cm)	14.198
Inlet length (cm)	60.0
Heated length (cm)	80.0
Outlet length (cm)	20.32
Outlet pressure (Pa)	7.58e5
Outlet gauge pressure (Pa)	0.0
Inlet temperature (K)	628.15
Axial power profile (-)	Chopped cosine (peaking factor 1.21)
Radial power profile (-)	Internal rings 1–2 heated
Linear pin power (W/cm)	241.9
Inlet flow rate (m^3/s)	7.164e-4
Mixing grid positions (cm)	(20, 80)

Table 11: Design and operational parameters for the conceptual ABTR fuel assembly for low-flow case.

the assembly. The flow accelerates until the end of the heated section at 1.4-m high. Then, without buoyancy forces, the flow in the center has a larger pressure leading to flow redistribution to the outer channels and reversing its axial direction. Flow continues to descend next to the outer channels until it gets goes back into the center subchannels and ascends again. These phenomena result in a large temperature peak at the center of the assembly with a hot region next to this temperature peak due to the heated descending flow. A small asymmetry if observed in the cross flows. This is mainly a product of the way in which the pressure drop sweep coefficients have been defined in which all wire spacers are considered to start at the same angle at the bottom of the assembly. Results may be different is a different wire-spacer configuration is utilized. Analyzing the temperature field for the radial mid-height cut, one can observe that the outer part of the ring is slightly hotter than its surroundings. This is a product of two effects. First, the outer subchannel presents a smaller pressure drop than the center subchannels, which results in these channel needing a smaller buoyancy force to achieve equivalent flow rates than the center subchannels. Second, there is a small heating effect due to heat conduction in the duct. The total temperature rise in the fuel assembly is $\sim 130K$, which is similar to the $129K$ predicted by the enthalpy balance

without accounting for duct heating.

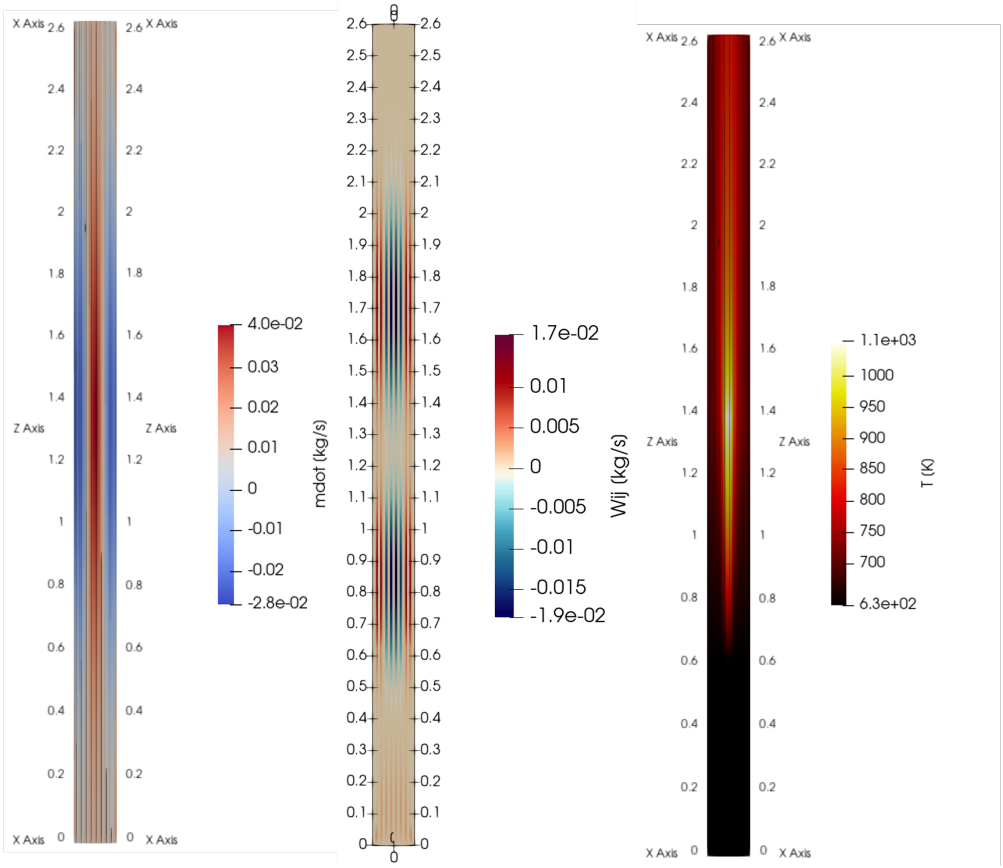

Figure 28: Axial cut of the thermal-hydraulics fields obtained for the low-flow study; left: axial mass flow rate; center: sum of lateral mass flow rate per subchannel; right: temperature.

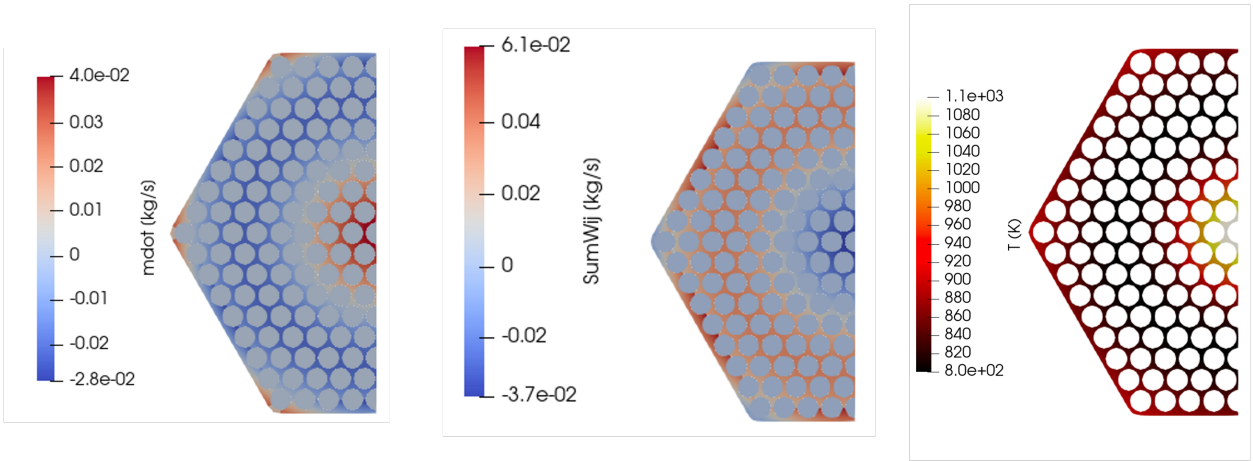

Figure 29: Radial cut of the thermal-hydraulics fields obtained for the high-flow study at $z = 1.3$ m; left: axial mass flow rate; center: sum of lateral mass flow rate per subchannel; right: temperature.

In this section, we have demonstrated the ability of our subchannel code to simulate flow recirculation in low flow assemblies. Note that this only demonstrates that the numerical discretization implemented can handle flow recirculation. It does not mean that our code is validated or even numerically benchmarked for flow with recirculations. Code benchmarking and validation for this type of flows will be a future task.

7.4 Transient Analysis of Pin Power Burst in a Fuel Assembly of the 217-Pin Model

This section demonstrates the transient capabilities of PrSub. The transient problem is a power burst in the central pin of the fuel element. The subchannel assembly is assumed to be generating zero power at high flow conditions. This represents, for example, the conditions obtained in a hot shutdown. Then, at time $t = 0$ s, we introduce a power burst into the central pin. The power distribution for the central pin as a function of time is presented in Figure 30. This distribution consists of a chopped sine function that extends until time $t = 10\ s$. This problem is a simple test case to demonstrate the code's ability to deal with rapid transients. However, its intent is to loosely emulate the positive reactivity insertion transient due to fuel compaction in one fuel pin during a hot shutdown condition [38]. The setup for the transient simulation is detailed in Table 12.

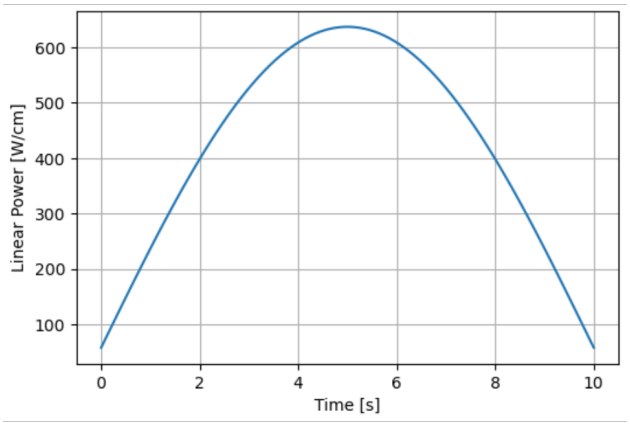

Figure 30: Linear power in the central pin as a function of time.

The transient distribution of temperature and mass fluxes in the subchannels during the transient are presented in Figures 31 and 32, respectively. Coolant circulates from bottom to top of

Experiment Parameter (unit)	Value
Number of pins (-)	217
Rod pitch (cm)	0.681
Rod diameter (cm)	0.603
Wire wrap diameter (cm)	0.103
Wire wrap axial pitch (cm)	20.23
Flat-to-flat duct distance (cm)	14.198
Inlet length (cm)	60.0
Heated length (cm)	80.0
Outlet length (cm)	20.32
Outlet pressure (Pa)	7.58e5
Outlet gauge pressure (Pa)	0.0
Inlet temperature (K)	628.15
Axial power profile (-)	Uniform with amplitude function
Radial power profile (-)	Only central pin is heated
Linear pin power (W/cm)	241.9
Inlet flow rate (m^3/s)	2.388e-2
Mixing grid positions (cm)	(20, 80)

Table 12: Design and operational parameters for the conceptual ABTR fuel assembly transient simulation.

the fuel assembly. The temperature increases as the power in the central pin increases and, then, decreases while the power goes down. There is an observable lag in the temperature evolution in the subchannels after the pin power reaches its peak due to the thermal inertia in the pin and the subchannel system. Regarding axial flows, the axial flow in the central channels increases as they are heated by the central pin power burst. The hotter temperature in the center of the subchannel reduces flow viscosity, which, in turn, reduces the pressure drop in this region. This causes flow to migrate from the outer channels into the inner ones, as can be observed in the mid-height radial cuts presented in Figure 33 for the lateral cross-flows. Finally, the system relaxes back to the original condition as power in the central pin decreases.

As observed in Figure 31, the temperature in the outer subchannels also increases axially. This is in part the effect of radial heat diffusion in the liquid sodium subchannels, but it is also produced by the heating because of the wrapper that is now considerably hotter than the subchannels. The outer wall of the duct in these simulations is still imposed the temperature profile from 37-element full power model, Section 6.2, which is significantly hotter than the one obtained in the hot shutdown assembly. This causes the heating of the external subchannels by thermal conduction.

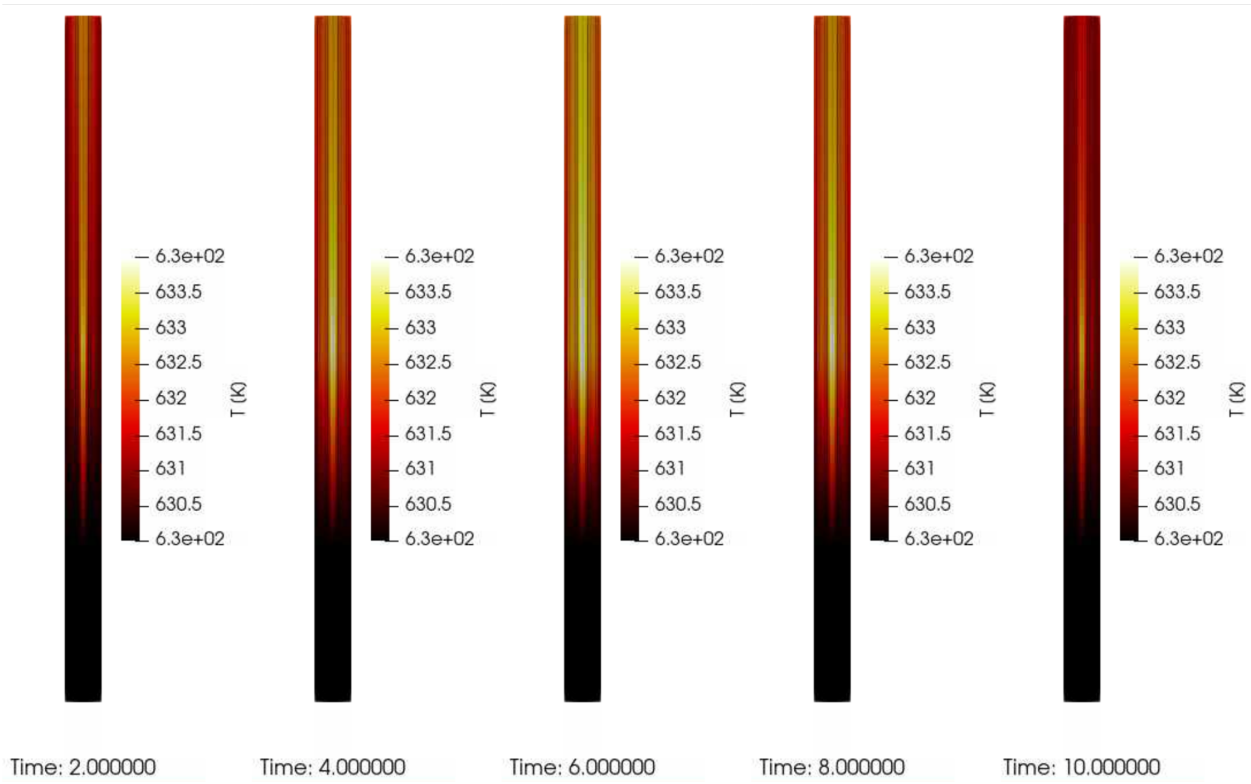

Figure 31: Evolution of the temperature in the subchannels as a function of time due to the power burst in the center pin.

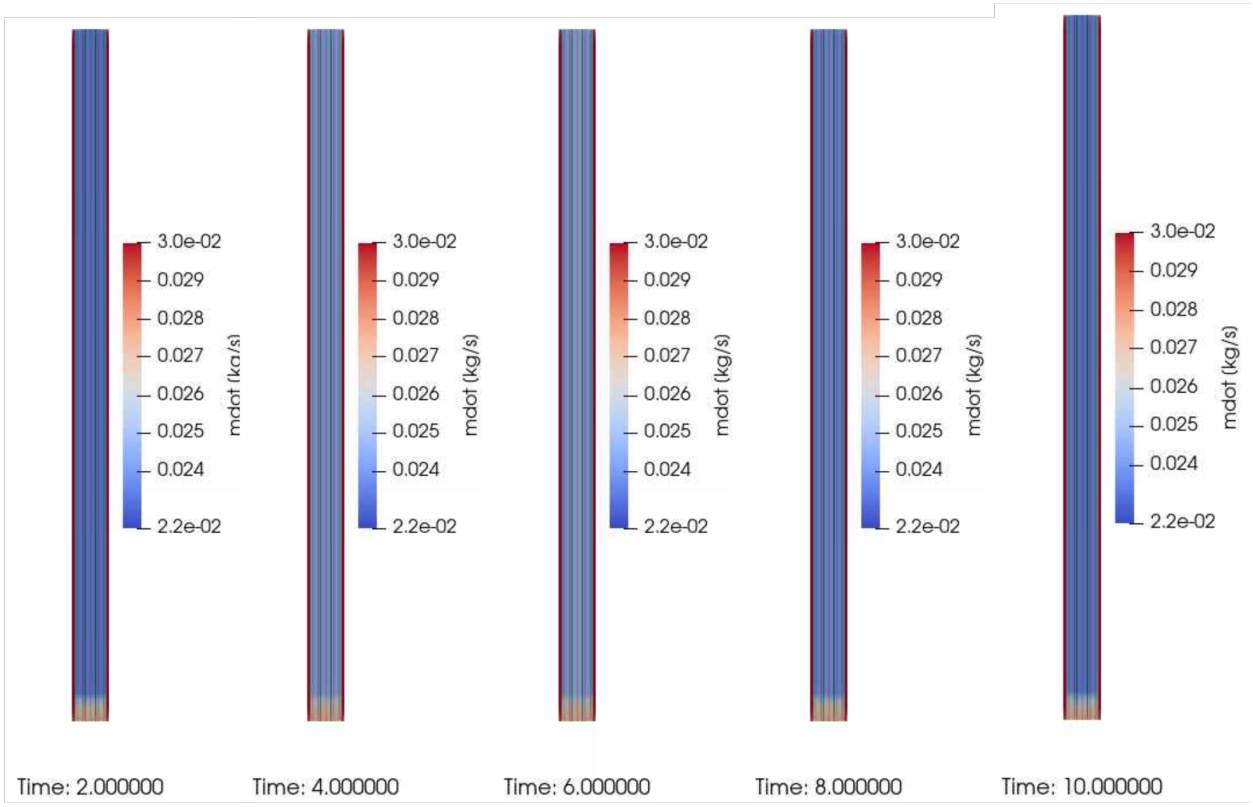

Figure 32: Evolution of the axial mass flow rate in the subchannels as a function of time due to the power burst in the center pin.

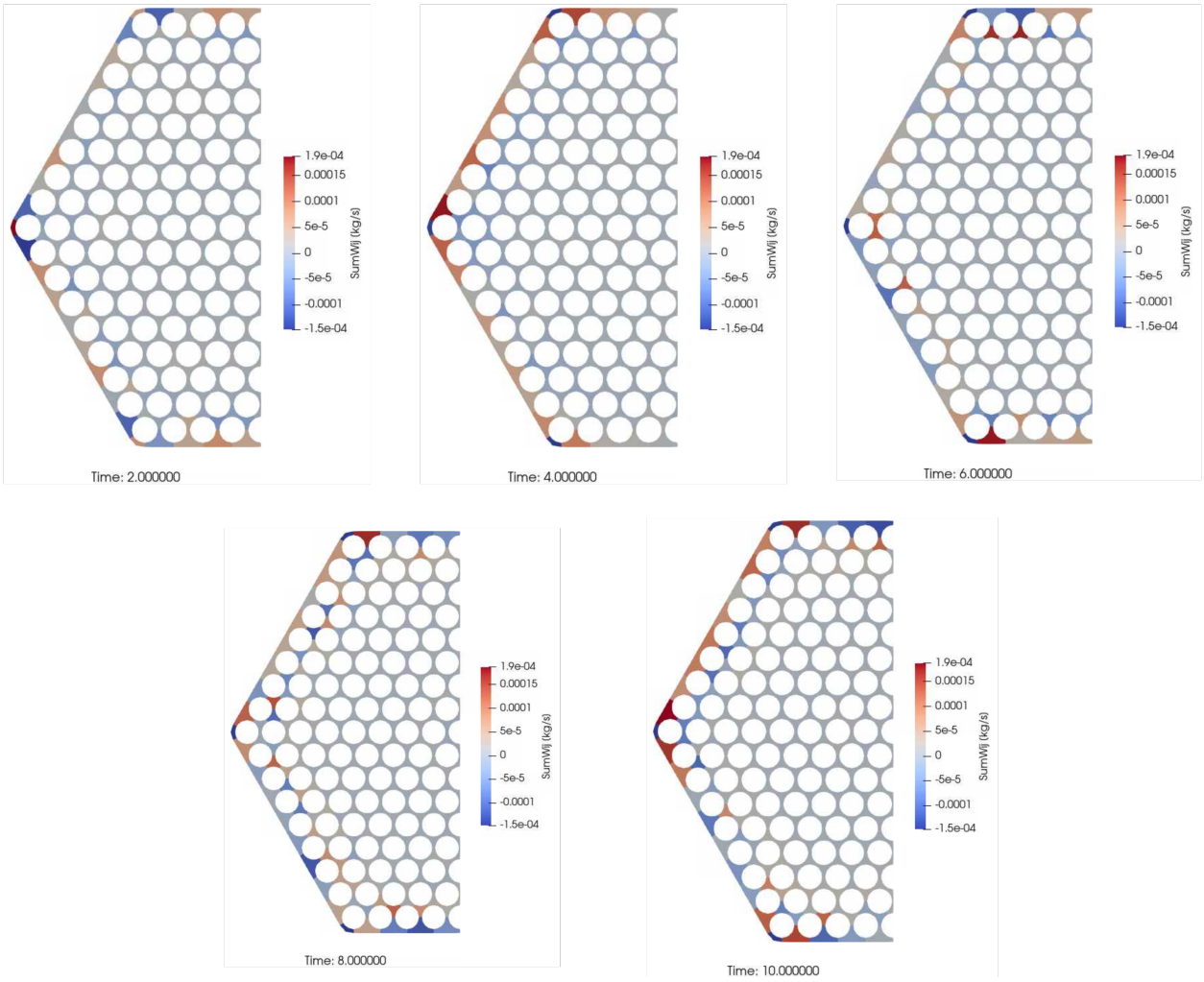

Figure 33: Evolution of the lateral mass flow rate in the subchannels as a function of time due to the power burst in the center pin.

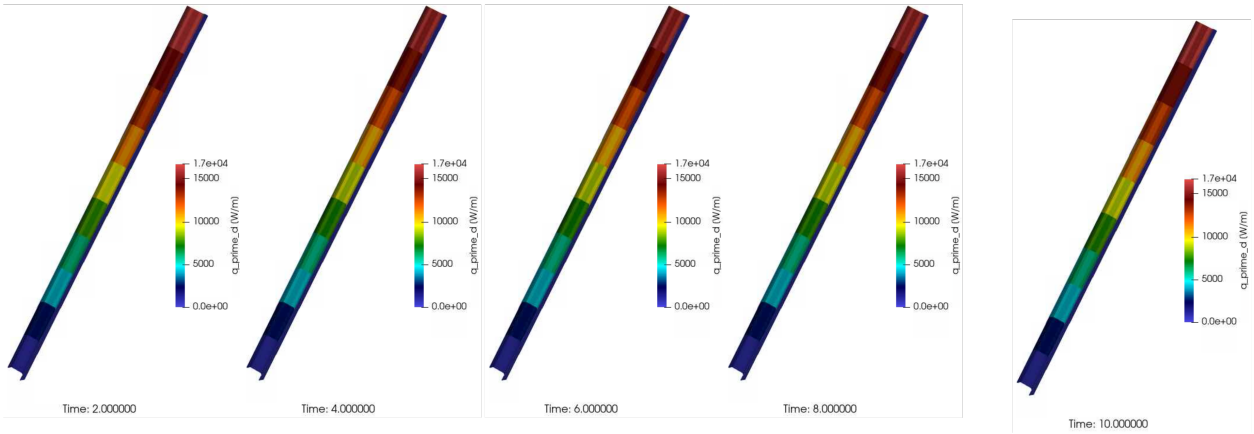

Figure 34: Evolution of heat flux coming from the duct into the subchannels during the transient.

The heat fluxes from the duct into the subchannels are presented in Figure 34. The heat fluxes increase from bottom to top as the temperature of the outside wrapper increases more rapidly than the temperature in the subchannel assembly.

In this section, we have demonstrated the capability of the coupled simulations to compute the transient phenomena obtained in an SFR assembly. Further testing and VBV of the transient models will be developed in future work.

7.5 Online Coupling of PrSub with Pronghorn Porous Flow Models

In this section, we demonstrate the online coupling of PrSub and Pronghorn's porous flow model. We simplify the seven-element model described in Section 6 by assuming that the seven outer assemblies have no heat source, so we can drop the solid energy equation in that domain. The central assembly is modeled using PrSub, while the six outer assemblies are modeled using porous flow. The duct and inter-wrapper spaces are solved alongside the porous flow model in the same same way as described in Section 6.

The conjugate heat transfer from the duct to the inter-wrapper space and from the duct to the six outer assemblies is modeled using Robin boundary conditions, see Equation 69. The heat transfer from the PrSub domain to the heat conduction problem in the duct is accomplished by using a mixed Neumann-Dirichlet approach. Dirichlet temperature boundary conditions computed by PrSub are applied to the inside of the duct on the heat conduction side, while PrSub uses Neumann boundary conditions with heat fluxes computed by the heat conduction

solve. We apply fixed velocity inlet boundary conditions of 0.1, 1.5, and 3.5 m/s at the inlet of the inter-wrapper, outer assemblies, and central assembly. The central assembly has a uniform radial pin power (all pins are identical) and an axial power shape given by:

$$p(z) \propto \begin{cases} \sin\left(\frac{z-0.6}{0.8}\pi\right) & \text{if } z > 60 \text{ and } z < 140; \\ 0 & \text{else.} \end{cases} \tag{93}$$

The total power applied to the central assembly is 5.7 MW.

The coupled simulation is set up using the MultiApp system. PrSub is the primary app, while the heat conduction and porous flow solve are the secondary apps. In this work, we only show steady-state results obtained using a pseudo-transient (time stepping until steady-state is achieved). Therefore, the two apps are coupled loosely equivalent to only doing a single Picard iteration. This does not have any numerical consequences because the time stepping essentially forms the Picard loop for achieving consistency at the final steady-state conditions.

We present a radial slice of the steady-state temperature distribution for the described problem in Figure 35 at $z = 2$ m (located about 0.6 m above the upper end of the heated section). The central assembly heats to more than 1000 K, driven by the excess power provided to it. Heat is transferred from the inside assembly to the duct around it and then via heat conduction and conjugate heat transfer into the inter-wrapper flow, and from the inter-wrapper flow into to the neighboring ducts and on to the porous flow regions. The portion of the outside ducts that face the inner fuel element heat to about 800 K, while the fluid temperature in the outside assemblies stays well below 650 K. The fluid temperature in the inter-wrapper space is largest close to the center of the edges of the hexagonal fuel channels and reduces towards the corners. This is because the flow redistributes from the channels around the central fuel element into the neighboring flow channels near the corners, reducing the temperature in these regions. The temperatures in the outside ducts near these corners are larger than the fluid temperature. This is driven by heat conduction from the hotter region close to the center of the edge. Overall, the temperature distribution appears physically reasonable. Nevertheless, we recommend a further assessment of the results.

The simulation results are presented for demonstration purposes only. The selected test case is not very realistic, and results have not been extensively assessed. Additional work will also be

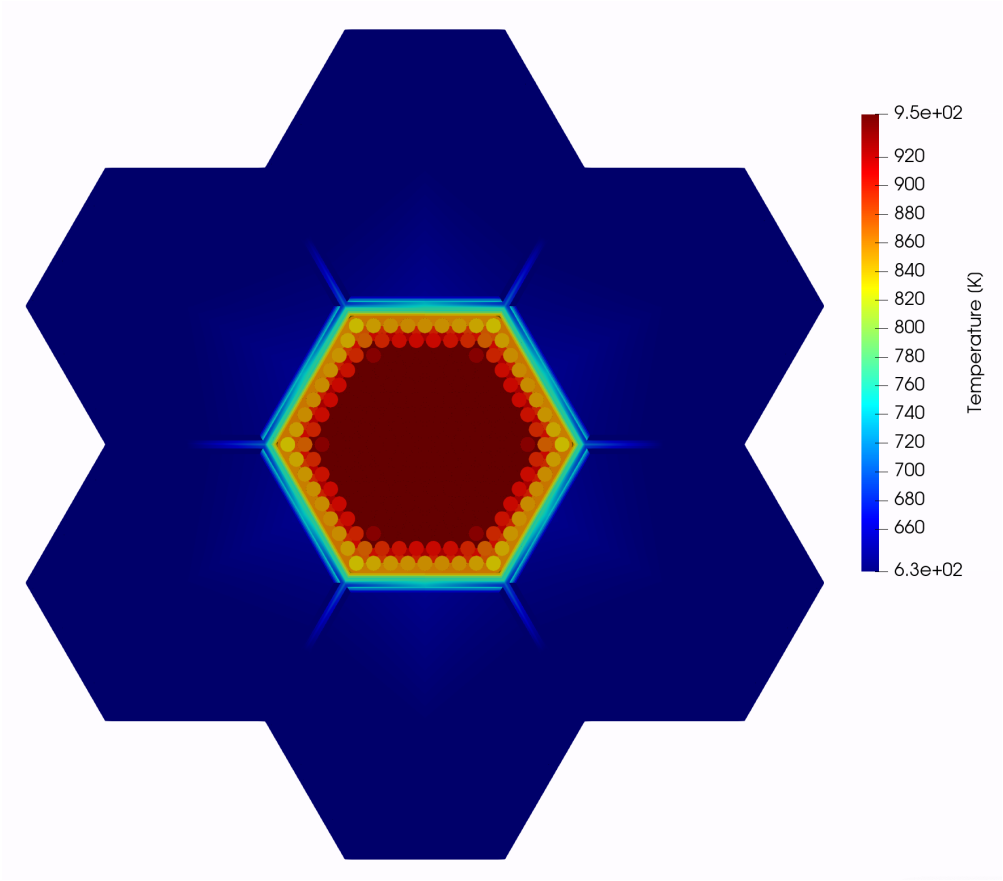

Figure 35: Temperature distribution for the seven-element coupled PrSub and porous flow simulation at an axial slice at $z = 2$ m above the inlet.

performed by this group to make the coupling more user-friendly, efficient, and robust.

8. Summary

Here we report the completion of the first phase of development of a comprehensive modeling capability for engineering-scale thermal-hydraulics in LMFRs. Two different approaches for modeling LMFRs were developed: (1) a subchannel capability supporting hexagonal fuel elements implemented in PrSub and (2) a porous flow method based on Pronghorn's FVM capability. These two methods are inter-operable with each other and with most other existing MOOSE capabilities. This opens the door for mixed porous flow and subchannel coupled with any of the multiphysics capabilities already present in MOOSE.

PrSub is an efficient subchannel code (problems with several 100,000 DoF require about 90 seconds of execution time per time step) with a robust numerical solver that allows the simulation of steady-state and transient problems. We demonstrate that the solver is robust enough to handle non-standard flow conditions, such as a flow reversal in high-buoyancy, low-flow fuel elements.

We demonstrated that the FVM porous flow solver in Pronghorn allows effective modeling of flow paths with engineered orifices and the computation of the flow field in the fuel assemblies and the inter-wrapper spaces. The flow model is fully coupled with the heat conduction in the pins and ducts via conjugate heat transfer. The ability to model flow in the inter-wrapper space has the potential to improve on the common approach to model inter-wrapper spaces using effective thermal conductivities.

We showed that PrSub can be combined with MOOSE's ability to compute flow conditions in the inter-wrapper space, temperatures in the duct, and conjugate heat transfer between subchannel and inter-wrapper flow spaces to determine temperature distributions in the ducts. These duct temperatures are important for the design and licensing of LMFRs.

In summary, we have demonstrated the following capabilities in this report:

- Implementing and V&V of closure relations for hexagonal lattices
- Coupling the subchannel flow model to multidimensional FEM or FVM heat conduction models and iterating to consistency via fixed point iterations.
- Developing closure relationships for modeling LMFRs using Pronghorn's porous media FVM approach

- Modeling LMFRs using a mixed porous flow FVM and subchannel approach
- Explicitly modeling inter-wrapper flows along with conjugate heat transfer from the intra-element flow to the duct and from the duct to the inter-wrapper flow using Pronghorn's FVM capabilities
- Modeling special assemblies, such as double-ducted control assemblies using Pronghorn's FVM porous flow model, using a simple concentrated pressure drop approach
- Scaling up to about 37 assemblies discretized with about $120,000$ elements in a three-dimensional geometry using Pronghorn's FVM solver, though increasing the problem size requires removing current inefficiencies in the FVM solution algorithm.

Future work will focus on improving the MOOSE-based LMFR capabilities by:

- Improving the performance of the FVM porous flow solvers by deploying the MOOSE native segregated solver
- Making the coupling between the subchannel, heat conduction, and FVM porous flow more user-friendly
- Completing VBV to increase the credibility of the capabilities we developed in this work.

REFERENCES

[1] N. E. Todreas and M. S. Kazimi, *Nuclear Systems II: Elements of thermal Hydraulic design*. Taylor and Francis., 2001.

[2] AREVA, *COBRA-FLX: A Core Thermal-Hydraulic Analysis Code Topical Report*. AREVA NP Inc., 2010.

[3] V. Kyriakopoulos, M. E. Tano, and J. C. Ragusa, "Development of a single-phase, transient, subchannel code, within the moose multi-physics computational framework," *Energies*, vol. 15, no. 11, 2022.

[4] Y. Chang, P. Finck, C. Grandy, J. Cahalan, L. Deitrich, F. Dunn, D. Fallin, M. Farmer, T. Fanning, T. Kim, *et al.*, "Advanced burner test reactor preconceptual design report.," tech. rep., Argonne National Lab.(ANL), Argonne, IL (United States), 12 2008.

[5] Y. Yu, E. Merzari, A. Obabko, and J. Thomas, "A porous medium model for predicting the duct wall temperature of sodium fast reactor fuel assembly," *Nuclear Engineering and Design*, vol. 295, pp. 48–58, 2015.

[6] C. J. Permann, D. R. Gaston, D. Andrš, R. W. Carlsen, F. Kong, A. D. Lindsay, J. M. Miller, J. W. Peterson, A. E. Slaughter, R. H. Stogner, and R. C. Martineau, "MOOSE: Enabling massively parallel multiphysics simulation," *SoftwareX*, vol. 11, p. 100430, 2020.

[7] A. J. Novak, R. W. Carlsen, S. Schunert, P. Balestra, D. Reger, R. N. Slaybaugh, and R. C. Martineau, "Pronghorn: A multidimensional coarse-mesh application for advanced reactor thermal hydraulics," *Nuclear Technology*, vol. 207, no. 7, pp. 1015–1046, 2021.

[8] R. L. Williamson, J. D. Hales, S. R. Novascone, G. Pastore, K. A. Gamble, B. W. Spencer, W. Jiang, S. A. Pitts, A. Casagranda, D. Schwen, A. X. Zabriskie, A. Toptan, R. Gardner, C. Matthews, W. Liu, and H. Chen, "Bison: A flexible code for advanced simulation of the performance of multiple nuclear fuel forms," *Nuclear Technology*, vol. 207, no. 7, pp. 954–980, 2021.

[9] R. L. Williamson, J. Hales, S. Novascone, M. Tonks, D. Gaston, C. Permann, D. Andrs, and R. Martineau, "Multidimensional multiphysics simulation of nuclear fuel behavior," *Journal of Nuclear Materials*, vol. 423, no. 1-3, pp. 149–163, 2012.

[10] D. A. Knoll and D. E. Keyes, "Jacobian-free newton–krylov methods: a survey of approaches and applications," *Journal of Computational Physics*, vol. 193, no. 2, pp. 357–397, 2004.

[11] J. Ortensi, Y. Wang, V. M. Laboure, Z. M. Prince, C. Lee, Y. S. Jung, H. Park, and E. R. Shemon, "Griffin software development plan,"

[12] D. R. Gaston, C. J. Permann, J. W. Peterson, A. E. Slaughter, D. Andrš, Y. Wang, M. P. Short, D. M. Perez, M. R. Tonks, J. Ortensi, L. Zou, and R. C. Martineau, "Physics-based multiscale coupling for full core nuclear reactor simulation," *Annals of Nuclear Energy*, vol. 84, pp. 45–54, 2015.

[13] F. M. White, *Fluid mechanics*. Tata McGraw-Hill Education, 1979.

[14] B. Pang, *Numerical study of void drift in rod bundle with subchannel and CFD codes*. KIT, 2013.

[15] S.-K. Cheng and N. E. Todreas, "Hydrodynamic models and correlations for bare and wire-wrapped hexagonal rod bundles—bundle friction factors, subchannel friction factors and mixing parameters," *Nuclear engineering and design*, vol. 92, no. 2, pp. 227–251, 1986.

[16] S. Chen, Y. Chen, and N. Todreas, "The upgraded cheng and todreas correlation for pressure drop in hexagonal wire-wrapped rod bundles," *Nuclear Engineering and Design*, vol. 335, pp. 356–373, 2018.

[17] S.-k. Cheng *et al.*, *Constitutive correlations for wire-wrapped subchannel analysis under forced and mixed convection conditions*. PhD thesis, Massachusetts Institute of Technology, 1984.

[18] J. M. Bates and E. U. Khan, "Investigation of combined free and forced convection in a 2 x 6 rod bundle during controlled flow transients," 10 1980.

[19] S. Balay, S. Abhyankar, M. Adams, J. Brown, P. Brune, K. Buschelman, L. Dalcin, A. Dener, V. Eijkhout, W. Gropp, *et al.*, "Petsc users manual," 2019.

[20] E. Merzari, H. Yuan, M. Min, D. Shaver, R. Rahaman, P. Shriwise, P. Romano, A. Talamo, Y.-H. Lan, D. Gaston, R. Martineau, P. Fischer, and Y. Hassan, "Cardinal: A lower-length-scale multiphysics simulator for pebble-bed reactors," *Nuclear Technology*, vol. 207, no. 7, pp. 1118–1141, 2021.

[21] C. Fiorina, I. Clifford, M. Aufiero, and K. Mikityuk, "Gen-foam: a novel openfoam® based multi-physics solver for 2d/3d transient analysis of nuclear reactors," *Nuclear Engineering and Design*, vol. 294, pp. 24–37, 2015.

[22] A. Lindsay, M. Tano, G. Giudicelli, P. German, and S. Schunert, "Improvement of numerical methods in pronghorn," Tech. Rep. INL/EXT-21-65482, Idaho National Laboratory, 2021.

[23] K. Rehme, "Pressure drop correlations for fuel element spacers," *Nuclear Technology*, vol. 17, no. 1, pp. 15–23, 1973.

[24] E. Khan, W. Rohsenow, A. Sonin, and N. Todreas, "A Porous Body Model for Predicting Temperature Distribution in Wire-Wrapped Fuel Rod Assemblies ," *Nuclear Engineering and Design*, vol. 35, pp. 1–12, 1975.

[25] R. Gajapathy, K. Velusamy, P. Selvaraj, P. Chellapandi, S. Chetal, and T. Sundararajan, "Thermal Hydraulic Investigations of Intermediate Heat Exchanger in a Pool-Type Fast Breeder Reactor," *Nuclear Engineering and Design*, vol. 238, pp. 1577–1591, 2008.

[26] K. Mikityuk, "Heat Transfer to Liquid Metal: Review of Data and Correlations for Tube Bundles," *Nuclear Engineering and Design*, vol. 239, pp. 680–687, 2009.

[27] C. Hsu, "Analytical Study of Heat Transfer to Liquid Metals in Cross-Flow Through Rod Bundles," *International Journal of Heat and Mass Transfer*, vol. 7, pp. 431–446, 1964.

[28] J.-H. EOH, J.-W. HAN, S.-O. KIM, and J.-E. CHA, "Effect of heat transfer correlations of a channel sodium flow on thermal sizing of sodium-to-sodium heat exchangers," in *Transactions of the Korean Nuclear Society Autumn Meeting*, Korean Nuclear Society, 2010.

[29] E. Shemon, Y. S. Jung, S. Kumar, Y. Miao, K. Mo, A. Oaks, and S. Richards, "Moose framework meshing enhancements to support reactor analysis," techreport, Argonne National Laboratory, ANL/NSE-21/43, Sept. 2021.

[30] R. Moreno, "A parametric study on core performance of sodium fast reactors using serpent code," Master's thesis, Royal Institute of Technology, Stockholm, 2.

[31] G. Caruso, "Esercitazioni di impianti nucleari," Aracne, 2003.

[32] I. E. Idelchik, "Handbook of hydraulic resistance," *Washington*, 1986.

[33] C. G. Robert Salko, Marcus Gergar and M. Avramova, *CTF Void Drift Validation Study*. CASL, 2015.

[34] M. Fontana, R. MacPherson, P. Gnadt, L. Parsly, and J. Wantland, "Temperature distribution in the duct wall and at the exit of a 19-rod simulated lmfbr fuel assembly (ffm bundle 2a)," *Nuclear Technology*, vol. 24, no. 2, pp. 176–200, 1974.

[35] R. Sun, D. Zhang, Y. Liang, M. Wang, W. Tian, S. Qiu, and G. Su, "Development of a subchannel analysis code for sfr wire-wrapped fuel assemblies," *Progress in Nuclear Energy*, vol. 104, pp. 327–341, 2018.

[36] W.-S. Kim, Y.-G. Kim, and Y.-J. Kim, "A subchannel analysis code matra-lmr for wire wrapped lmr subassembly," *Annals of Nuclear Energy*, vol. 29, no. 3, pp. 303–321, 2002.

[37] F. Namekawa, A. Ito, and K. Mawatari, "Buoyancy effects on wire-wrapped rod bundle heat transfer in an lmfbr fuel assembly," in *AIChE symposium series*, vol. 80, pp. 128–133, 1984.

[38] I. Pioro, *Handbook of generation IV nuclear reactors*. Woodhead Publishing, 2016.